

Neutron stars with primary scalar hair

Hamza Boumaza^a, Christos Charmousis^b, David Langlois^c, and Etienne Ligout^{c,d}

^a*Laboratoire de Physique des Particules et Physique Statistique (LPPPS), Ecole Normale Supérieure-Kouba, B.P. 92, Vieux Kouba, 16050 Algiers, Algeria*

^b*Université Paris-Saclay, CNRS/IN2P3, IJCLab, 91405 Orsay, France*

^c*Université Paris Cité, CNRS, Astroparticule et Cosmologie, F-75013 Paris, France*

^d*Sorbonne Université, CNRS, Institut d'Astrophysique de Paris, G \mathbb{R} ϵ CO, 75014 Paris, France*

July 3, 2026

Abstract

We investigate static and spherically symmetric neutron star solutions endowed with primary scalar hair in a subfamily of Degenerate-Higher-Order-Scalar-Tensor (DHOST) theories of gravity. By solving the modified Tolman-Oppenheimer-Volkoff (TOV) equations, we construct equilibrium configurations for polytropic and realistic equations of state and analyse the impact of the scalar hair on the stellar structure. We examine the resulting metric and scalar field profiles as well as the mass-radius relation, showing deviations from the predictions of General Relativity (GR). Positive scalar charges lead to more compact stars than in GR and, above a critical threshold, to singularities. Observations could therefore put stringent constraints on the parameters characterising the beyond-GR effects in these theories and their potential scalar hair.

Contents

1	Introduction	2
2	Model and previous solutions	3
2.1	DHOST theories, general Lagrangian	4
2.2	Black hole solutions	4
3	Equations of motion	7
3.1	Reduced action and equations of motion	7
3.2	Impact of the scalar field	9
3.3	Characteristic properties and singularity for the neutron star interior	10
4	Numerical analysis	12
4.1	Neutron star structure for a polytropic equation of state	12
4.2	Phenomenological equations of state	16
4.3	Mass-radius relation	19
4.4	Case of negative scalar charge	22
5	Conclusions	24
A	Expansion near the center of the equations of motion	26
B	Coefficients b_i for the analytic expression of realistic equations of states	27

1 Introduction

Strong gravity manifests itself in compact objects, such as black holes and neutron stars, making them ideal arenas for testing General Relativity (GR) and exploring alternative theories of gravity. In recent years a wealth of observational data on compact objects has been collected by gravitational-wave (GW) detectors [1, 2], networks of radio-telescopes like the Event Horizon Telescope [3] and X-ray telescopes such as NICER [4]. Observational data will be greatly enhanced in the near future with far better precision as well as novel instruments such as the Einstein Telescope [5] or the Laser Interferometer Space Antenna (LISA) [6].

While current data remain compatible with GR within observational uncertainties, it is crucial to anticipate potential effects beyond GR. This preparation is essential both for interpreting the upcoming plethora of data and for exploring alternative scenarios motivated by open questions or existing tensions. Beyond direct consistency checks of GR [7], important questions remain to be answered, such as the equation of state (EoS) of high-density nuclear matter, the maximum mass of neutron stars, their maximum rotation, etc. Furthermore, certain tensions with observations exist. For example recent observations of compact binaries such as GW190814 [8], GW200210 or GW230529 [9] give primary or secondary compact objects with a mass well within the mass gap interval between 2 and 5 M_\odot predicted in astrophysical processes in GR. In the case of GW190814, the secondary component of the binary has a mass of $2.59^{+0.08}_{-0.09} M_\odot$. Within GR, this could only be explained by a neutron star with an unexpectedly stiff (or exotic) EoS, an unusually rapidly rotating neutron star or a black hole with a surprisingly small mass (see for example [10–15]).

Many theories of modified gravity are based on the inclusion of a scalar field in the gravitational sector, in addition to the usual metric field. The most general scalar-tensor theories propagating a single

scalar degree of freedom are known as Degenerate-Higher-Order-Scalar-Tensor (DHOST) theories¹ [16–18] (see [19, 20] for reviews), which include well studied theories such as the traditional scalar-tensor theories, Horndeski theories and Einstein-scalar-Gauss-Bonnet theories. Recently, new static black hole (BH) solutions — characterised by primary hair — have been discovered [21] (see also [22, 23]) within the framework of DHOST theories. These BH solutions represent a one-parameter deformation of the traditional Schwarzschild metric, together with a non-trivial scalar field profile. The primary scalar hair of these solutions is due to a global shift symmetry of the action which is translated in a linear time dependence for the scalar field [24]. This not only gives an independent scalar hair but also renders the scalar field regular at the event horizon of the black hole.

The extension of these static black holes to slow rotation was recently achieved in [25], while theoretical studies on their intriguing thermodynamic properties were initiated in [26–28]. More phenomenological aspects such as strong lensing and shadow analyses, were recently explored in [29, 30]. Linear perturbations of these solutions, in particular quasinormal modes, were investigated in [31–35], while axial and radial perturbations around these backgrounds were studied in [36, 37].

In this work, we extend the study of the same subfamily of DHOST theories to relativistic stars — typically neutron stars. While the exterior of these stars matches that of the BH solutions reported in [21], the presence of matter modifies their interior. To compute the star’s interior profile, we derive generalised Tolman-Oppenheimer-Volkoff (TOV) equations that incorporate the effects of the gravitational scalar field. Interestingly, we find that these modified gravity effects are encapsulated in a radially-dependent effective perfect fluid with equation of state $P_{\text{eff}} = -\rho_{\text{eff}}$. As a consequence, for the same central density of baryonic matter, the mass and the radius of the star differ from their GR counterparts. For a given DHOST theory, all these modifications depend on a theory-dependent length parameter and on the effective scalar charge of the star. By integrating the modified TOV equations, we obtain numerical solutions that represent one-parameter deformations of GR neutron stars, characterised solely by their central density and EoS.

Starting with the well-known scalarisation mechanism proposed in [38], numerous investigations of relativistic stars within different distinct subfamilies of DHOST theories have been reported in the literature (see e.g. [39–52]). For a particular class of Horndeski theories [53–55] it was found in [56] that neutron stars could acquire a larger mass than in GR (such as that observed in certain GW binaries [8, 9]) without requiring a stiffer EoS. Our study also exhibits this property, but with a key difference: in our model, a more massive star requires a positive scalar charge, whereas in [56], it required a positive coupling constant. In other words, the fixed coupling constant in the earlier theory is replaced here by a free parameter — the primary hair.

The outline of our paper is the following. In the next section, we introduce the subfamily of DHOST theories we will focus on and recall the recently discovered BH solutions with primary scalar hair in this framework. We then derive, in Section 3, the modified TOV equations governing a static and spherically symmetric configuration. In Section 4, we solve numerically the system of equations for a polytropic EoS and a few phenomenological EoS. We then give some conclusions and perspectives in the final section. Two appendices are added to provide some technical details.

2 Model and previous solutions

In this section, we present DHOST theories and review the static BH solutions with primary hair that will describe the exterior of our neutron star solutions. These black hole solutions have been discovered in [21] and, soon after, extended in [22, 23]. Their axial and radial perturbations and several other

¹Despite the presence of second-order derivatives of the scalar field in their Lagrangian, these theories avoid the presence of a ghost-like extra degree of freedom due to degeneracy relations satisfied by their Lagrangian functions.

properties were recently analysed in [36, 37], whose notation we adopt. We will in particular focus on the homogeneous² versions of these BH spacetimes since — as explicitly shown in [23, 36] — any non homogeneous solution belongs to an equivalence class which is connected to a homogeneous solution via a disformal transformation [57].

2.1 DHOST theories, general Lagrangian

We consider DHOST theories whose action contains up to quadratic terms in second derivatives of the scalar field. These theories are described by the action [16]

$$S[g_{\mu\nu}, \phi] = \frac{1}{2\kappa} \int d^4x \sqrt{-g} \left(P(X, \phi) + Q(X, \phi) \square\phi + F(X, \phi)R + \sum_{i=1}^5 A_i(X, \phi) L_i^{(2)} \right) \quad (2.1)$$

where $\kappa \equiv 8\pi G$ and the kinetic density is given by³

$$X \equiv -\frac{1}{2} \partial_\mu \phi \partial^\mu \phi. \quad (2.2)$$

The theory functions P , Q , F and A_i depend on ϕ and X , while the elementary quadratic Lagrangians read [16]

$$\begin{aligned} L_1^{(2)} &= \phi^{\mu\nu} \phi_{\mu\nu}, & L_2^{(2)} &= (\square\phi)^2, & L_3^{(2)} &= (\square\phi) \phi^\mu \phi_{\mu\nu} \phi^\nu, \\ L_4^{(2)} &= \phi^\lambda \phi_{\lambda\mu} \phi^{\mu\nu} \phi_\nu, & L_5^{(2)} &= (\phi^\mu \phi_{\mu\nu} \phi^\nu)^2, \end{aligned}$$

with the notation $\phi_\mu \equiv \nabla_\mu \phi$ and $\phi_{\mu\nu} \equiv \nabla_\nu \nabla_\mu \phi$. The functions F and A_i satisfy three degeneracy conditions, ensuring that the resulting theory contains only a single scalar degree of freedom and thus avoids Ostrogradski instabilities.

The theories discussed in this paper all belong to a sub-class of DHOST theories, known as Beyond Horndeski theories [58, 59], characterised by the conditions

$$A_2 = -A_1, \quad A_4 = -A_3 = \frac{A_1 + F_{,X}}{X}, \quad A_5 = 0, \quad (2.3)$$

which ensure that the degeneracy conditions are verified. This sub-class itself contains the Horndeski theories [60], which satisfy

$$A_2 = -A_1 = F_{,X}, \quad A_3 = A_4 = A_5 = 0. \quad (2.4)$$

From now on, we restrict our attention to Lagrangians in which $Q = 0$ and the remaining independent functions P , F and A_1 depend only on X . This implies that the theory possesses shift ($\phi \rightarrow \phi + \text{const}$) and parity ($\phi \rightarrow -\phi$) global symmetries.

2.2 Black hole solutions

We consider a general ansatz for static and spherically symmetric metrics, given by

$$ds^2 = -\mathcal{A}(r) dt^2 + \frac{dr^2}{\mathcal{B}(r)} + r^2 d\Omega^2, \quad d\Omega^2 = d\theta^2 + \sin^2\theta d\varphi^2. \quad (2.5)$$

²By homogeneous metric, we mean one such that $g_{tt} = -1/g_{rr}$, as in Schwarzschild.

³Be aware that one often encounters the alternative convention $X \equiv \partial_\mu \phi \partial^\mu \phi$.

Due to the global shift symmetry of the theory, the scalar field can acquire a linear time dependence,

$$\phi(t, r) = qt + \psi(r), \quad (2.6)$$

where q is an integration constant. The presence of this integration constant circumvents the requirements of no-hair theorems [43, 61] and gives rise to an independent primary hair. Indeed, the field equations in vacuum reduce to three simple independent equations [21]:

$$\frac{\mathcal{A}}{\mathcal{B}} = \frac{\gamma^2}{Z^2}, \quad (2.7)$$

$$r^2(PZ)_X + 2(FZ)_X \left(1 - \frac{q^2\gamma^2}{2Z^2X}\right) = 0, \quad (2.8)$$

$$2\gamma^2 \left(\mathcal{A}r - \frac{q^2r}{2X} \right)' = -r^2PZ - 2FZ \left(1 - \frac{q^2\gamma^2}{2Z^2X}\right) + \frac{q^2\gamma^2 X'r}{ZX^2} (2XF_X - F), \quad (2.9)$$

where⁴

$$Z \equiv -F - 2XA_1, \quad (2.10)$$

a subscript X denotes a derivative with respect to X and a prime a derivative with respect to the radial coordinate r . The three equations include an integration constant γ which we will fix to unity without loss of generality. Hence (2.7) dictates that homogeneous black holes, i.e. such that $\mathcal{A} = \mathcal{B}$, are only possible⁵ for $Z = -1$ while any other non-homogeneous solution will be parametrised by a non trivial Z . In principle, any non-homogeneous solution of a given theory can be formally related via a disformal transformation to a homogeneous solution of another theory [23, 36].

So let us concentrate on homogeneous solutions with $Z = -1$. The second equation above, Eq. (2.8), is an algebraic equation for X and effectively yields the scalar field profile, while (2.9) gives us the metric component. Using these integrability properties, explicit solutions have been obtained for a family of DHOST theories (2.1) whose associated functions⁶ take the form

$$P(X) = -\frac{2\alpha}{\lambda^2}X^p, \quad F(X) = 1 - 2XA_1(X), \quad A_1(X) = \frac{\alpha}{2}X^{p-1}, \quad A_3(X) = \frac{\alpha}{2}(2p-1)X^{p-2}, \quad (2.11)$$

while $A_2 = -A_1$, $A_4 = -A_3$ and $A_5 = 0$, thus belonging to beyond Horndeski theories according to (2.3). These theories are characterised by three parameters: p takes positive integer or half-integer values henceforth, α is a dimensionless coupling constant and λ is a constant with the dimension of length.

For this family of theories, the second field equation (2.8) leads to the following scalar field profile:

$$X_0 = \frac{q^2/2}{1 + (r/\lambda)^2} \quad \Longrightarrow \quad \psi'(r)^2 = \frac{q^2}{\mathcal{A}(r)^2} \left[1 - \frac{\mathcal{A}(r)}{1 + (r/\lambda)^2} \right]. \quad (2.12)$$

⁴In the Beyond Horndeski notation, as used in the original papers [21–23], (2.10) becomes $Z = -G_4 + 2XG_{4X} + 4X^2F_4$.

⁵Since the GR limit corresponds to $F = 1$, we choose the negative sign for Z , consistent with its definition (2.10).

⁶Using the Beyond Horndeski notation, we have

$$G_2(X) = -\frac{2\alpha}{\lambda^2}X^p, \quad G_4(X) = 1 - \alpha X^p, \quad F_4(X) = \frac{\alpha}{4}(2p-1)X^{p-2}.$$

The last equation (2.9) is a simple ordinary differential equation for the metric component \mathcal{A} . It can be solved for the family of theories (2.11) considered here and, using (2.12), one finds

$$\mathcal{A}(r) = 1 - \frac{2\mu}{r} - \xi_p \frac{2\lambda}{r} \Xi_p(r/\lambda), \quad \Xi_p(x) \equiv \int_0^x du \frac{u^2}{(1+u^2)^p}, \quad (2.13)$$

where μ is an integration constant (with dimension of length, since we work implicitly in units where $G = 1$ and $c = 1$) and ξ_p is a dimensionless parameter,

$$\xi_p \equiv \alpha(2p-1) \left(q^2/2\right)^p, \quad (2.14)$$

which can be interpreted as the “strength” of the scalar hair. The integral Ξ_p can be expressed in terms of a hypergeometric function [22, 23],

$$\Xi_p(x) = \frac{x^3}{3} {}_2F_1(3/2, p; 5/2; -x^2), \quad (2.15)$$

which reduces to standard functions for special values of p , as will be illustrated below. When $x \rightarrow +\infty$, Ξ_p behaves as

$$\Xi_p(x) = \frac{\sqrt{\pi}\Gamma(p-\frac{3}{2})}{4\Gamma(p)} + \mathcal{O}\left(\frac{1}{x^3}\right) + x^{-2p} \left(\frac{x^3}{3-2p} + \frac{p}{2p-1}x - \frac{p(1+p)}{2(1+2p)x} + \mathcal{O}\left(\frac{1}{x^3}\right) \right), \quad (2.16)$$

for $p \neq -1/2, 1/2, 3/2$ (the special case $p = 1/2$ is discussed below). In this asymptotic regime, it is convenient to combine the constant term of $\Xi_p(r/\lambda)$ with μ so as to define the constant

$$M \equiv \mu + \frac{\sqrt{\pi}\Gamma(p-\frac{3}{2})}{4\Gamma(p)} \xi_p \lambda \quad (p \neq -1/2, 1/2, 3/2), \quad (2.17)$$

which can be interpreted as the usual ADM mass of the solution.

In summary, setting

$$\check{\Xi}_p \equiv \frac{\mu - M}{\xi_p \lambda} + \Xi_p, \quad (2.18)$$

we have obtained a solution with primary hair, of the form

$$\mathcal{A}(r) = 1 - \frac{2M}{r} - \xi_p \frac{2\lambda}{r} \check{\Xi}_p(r/\lambda), \quad (2.19)$$

parametrised by the mass M and the constant ξ_p , which quantifies the deviation of the solution from the standard Schwarzschild metric (recovered in the limit $\xi_p = 0$). Note that the dimensionless coupling constant α only enters through its sign, since it combines with the primary hair parameter q to form the dimensionless constant ξ_p (defined in (2.14)), which can differ for every compact object. By contrast, the length scale λ , fixed by the theory, is universal and sets the characteristic scale at which the scalar field affects the geometry, as can be seen from the expression of X_0 in (2.12), suppressed for $r \gg \lambda$.

If $\xi_p > 0$ then the horizon of the black hole is more compact than that of a GR black hole with the same mass. As we increase the value of ξ_p (with fixed mass M), an inner horizon appears, while the event horizon continues to shrink, in a very similar fashion to an electric or magnetic Reissner-Nordstrom BH. For $p > 3/2$, one can also define a Noether charge associated with the shift symmetry (see [36]).

It is worth stressing that the solution (2.19) is not necessarily a black hole. Indeed, if the function \mathcal{A} does not vanish, the solution describes a naked singularity, or a soliton in the particular cases where

\mathcal{A} is regular at the origin. Since $\Xi_p(x) \simeq x^3/3$ when $x \rightarrow 0$, it is clear from (2.13) that the solution is regular for $\mu = 0$, i.e. when the mass M takes the particular value

$$M_p^{\text{reg}} \equiv \frac{\sqrt{\pi} \Gamma(p - \frac{3}{2})}{4 \Gamma(p)} \xi_p \lambda \quad (p \neq -1/2, 1/2, 3/2). \quad (2.20)$$

If \mathcal{A} vanishes for some finite radius, then the solution with the mass M_p^{reg} yields a regular black hole, i.e. devoid of singularity behind the horizon.

Throughout our study we will focus on the explicit example given by $p = 2$, which we now briefly describe. For $p = 2$, the theory is defined by the functions

$$P(X) = -\frac{2\alpha}{\lambda^2} X^2, \quad F(X) = 1 - \alpha X^2, \quad A_1(X) = \frac{\alpha}{2} X, \quad A_3(X) = \frac{3}{2} \alpha, \quad (2.21)$$

yielding the metric component

$$\mathcal{A}(r) = 1 - \frac{2M}{r} + \xi_2 \left(\frac{\pi/2 - \arctan \frac{r}{\lambda}}{r/\lambda} + \frac{1}{1 + \frac{r^2}{\lambda^2}} \right). \quad (2.22)$$

The solution becomes regular when the mass M takes the special value

$$M_2^{\text{reg}} = \frac{\pi}{4} \xi_2 \lambda, \quad (2.23)$$

which requires $\xi_2 > 0$. Interestingly, depending on the value of ξ_2 , the regular solution can be either a black hole, if $\xi_2 > 2.8$, or a soliton for smaller values of ξ_2 (see [36]).

Note that the above metric component (2.22) entails a deviation from standard gravity around a spherical object. A detection of this deviation, for example by measuring the motion of small objects *close to* a BH would in principle enable one to measure ξ_2 and λ . The BH mass (deduced from the attraction of *distant* objects by the BH) should then satisfy the consistency inequality $M_{\text{BH}} > (\pi/4)\xi_2\lambda$ because a smaller mass would correspond to a naked singularity.⁷

3 Equations of motion

3.1 Reduced action and equations of motion

A convenient way to derive the equations of motion is to compute the reduced action obtained by substituting the metric (2.5) into the action (2.1), with the choice of DHOST functions (2.11). After some integrations by parts, we get the action

$$S_{\text{grav}}[\mathcal{A}, \mathcal{B}, X] = \frac{2\pi}{\kappa} \int dt dr \sqrt{\frac{\mathcal{A}}{\mathcal{B}}} \left\{ 2(1 - \mathcal{B} - r\mathcal{B}') \right. \\ \left. + \alpha X^p \left[-2 \left(1 + \frac{r^2}{\lambda^2} \right) + 4\mathcal{B} - \frac{q^2 \mathcal{B}}{X \mathcal{A}} + 2r \left(\mathcal{B} \frac{\mathcal{A}'}{\mathcal{A}} + \mathcal{B}' + 2p \frac{X'}{X} \frac{\mathcal{B}}{\mathcal{A}} \left(\mathcal{A} + \frac{1-2p}{4p} \frac{q^2}{X} \right) \right) \right] \right\}.$$

The above gravitational action must be supplemented by the action S_{m} for the matter, which is assumed to be minimally coupled to the metric. The variation of S_{m} with respect to the metric defines the

⁷This is strictly true only for $\xi_2 < 2.8$. For higher values of ξ_2 , the inequality will be slightly different (see the phase diagram in [36]).

matter energy-momentum tensor $T^{\mu\nu}$. Here, we model the matter as a barotropic perfect fluid, which is a very good approximation for a neutron star, so that

$$T^{\mu\nu} \equiv \frac{2}{\sqrt{-g}} \frac{\delta S_m}{\delta g_{\mu\nu}} = (\rho + P)u^\mu u^\nu + P g^{\mu\nu}, \quad (3.1)$$

where ρ is the energy density and P the pressure. The conservation of the energy-momentum tensor,

$$\nabla_\mu T^\mu_\nu = 0, \quad (3.2)$$

yields, for the metric (2.5), the relation

$$P' = -\frac{\mathcal{A}'}{2\mathcal{A}}(\rho + P), \quad (3.3)$$

which is convenient to use instead of the angular components of the metric equations.

Varying the total action $S = S_{\text{grav}} + S_m$ with respect to \mathcal{A} and \mathcal{B} , we get

$$\mathcal{A}' = \frac{\mathcal{A}}{\mathcal{B}} \left[\frac{(1 - \mathcal{B})}{r} + \kappa r (P - \rho_{\text{eff}}) \right], \quad (3.4a)$$

$$\mathcal{B}' = \frac{1 - \mathcal{B}}{r} - \kappa r (\rho + \rho_{\text{eff}}), \quad (3.4b)$$

where we have regrouped all the beyond-GR terms in an effective energy density, defined by

$$\kappa \rho_{\text{eff}} \equiv \xi_p \bar{X}^{p-1} \frac{\mathcal{B}}{\mathcal{A} r} \left[\frac{\mathcal{A} \frac{\bar{X}}{\bar{X}_0} - \mathcal{B}}{(2p-1)r\mathcal{B}} - \frac{\bar{X}'}{\bar{X}} \right], \quad (3.5)$$

using the convenient normalized kinetic density \bar{X} , and its exterior value \bar{X}_0 (obtained from (2.12)):

$$X \equiv \frac{q^2}{2} \bar{X} \quad \Longrightarrow \quad \bar{X}_0 = \frac{1}{1 + \frac{r^2}{\lambda^2}}. \quad (3.6)$$

The system (3.4) together with (3.3) has exactly the same form as in GR, except that the usual matter density ρ is now replaced by $\rho + \rho_{\text{eff}}$, whereas the pressure is replaced by $P - \rho_{\text{eff}}$. This implies that the deviations from standard GR can be described as an effective perfect fluid energy-momentum tensor with equation of state

$$P_{\text{eff}} = -\rho_{\text{eff}}, \quad (3.7)$$

where both terms are radially dependent.

Finally, varying the action S with respect to X and eliminating the metric derivatives \mathcal{A}' and \mathcal{B}' using (3.4a) and (3.4b), we obtain

$$\bar{X} = \frac{\mathcal{B}}{\mathcal{A}} \Theta \bar{X}_0, \quad \Theta \equiv 1 - \frac{2p-1}{2p\mathcal{B}} r^2 \kappa (\rho + P), \quad (3.8)$$

which effectively extends the expression (2.12) to the interior of the star. Note that when $p > 1/2$ the effect of the star matter can render $\Theta < 0$ and therefore $\bar{X} < 0$, in stark contrast with BH solutions where $\bar{X} \equiv \bar{X}_0 > 0$.

Using (3.8), we can rewrite (3.5) in the form

$$\kappa \rho_{\text{eff}} \equiv -\xi_p \bar{X}^{p-1} \frac{\mathcal{B}}{\mathcal{A} r} \left[\frac{\kappa r (\rho + P)}{2p\mathcal{B}} + \frac{\bar{X}'}{\bar{X}} \right]. \quad (3.9)$$

The system (3.3)-(3.4) appears deceptively simple and hides the complexity arising from the scalar field's influence on the stellar profile. Indeed, according to (3.9) and (3.8), the quantity ρ_{eff} contains derivatives of \mathcal{A} and \mathcal{B} , which must be transferred to the left-hand side of the equations to properly formulate a first-order system. In the next subsection, we will explicitly disentangle these terms.

3.2 Impact of the scalar field

Before analysing in detail the new terms in the equations of motion, let us first substitute, as is traditional in GR (see for example [62]), the local mass function $m(r)$ for the metric component \mathcal{B} , so that

$$\mathcal{B} = 1 - \frac{2m(r)}{r}. \quad (3.10)$$

The equations (3.4a) and (3.4b) then become

$$m' = \frac{r^2}{2} \kappa(\rho + \rho_{\text{eff}}) \quad (3.11)$$

and

$$\frac{\mathcal{A}'}{\mathcal{A}} = \frac{2m + r^3 \kappa(P - \rho_{\text{eff}})}{r(r - 2m)}. \quad (3.12)$$

Substituting this latter equation into (3.3) and using (3.11) to replace ρ_{eff} by m' , we obtain the modified TOV equation⁸:

$$P' = -\frac{\rho + P}{r(r - 2m)} \left(m + \frac{\kappa}{2} r^3 (P + \rho) - m' r \right). \quad (3.14)$$

It now remains to evaluate \bar{X}' in the star interior from (3.8) in order to decrypt ρ_{eff} in full generality. Defining the quantity

$$\tau \equiv \xi_p \frac{(2p - 1)}{4p} \frac{r^2 \kappa(\rho + P)}{\mathcal{A}^2 (1 + r^2/\lambda^2)} \bar{X}^{p-2}, \quad (3.15)$$

we can rewrite the term proportional to the effective energy density on the right hand side of (3.11) in the form

$$\frac{r^2}{2} \kappa \rho_{\text{eff}} = \frac{\xi_p \bar{X}^p}{\lambda^2 \Theta} r^2 - \left(3 + \frac{1}{c_s^2} \right) \tau \left[\frac{m}{r} - m' + \frac{r^2 \kappa}{2} (\rho + P) \right] + \tau \left[3 \left(1 - \frac{2m}{r} \right) + \frac{r^2 \kappa}{2p} (\rho + P) \right], \quad (3.16)$$

where we have introduced the sound speed $c_s^2 \equiv P'/\rho'$. Having obtained ρ_{eff} in an expanded form, it is now straightforward to write down the modified field equations explicitly as a first order ODE system of three equations governing the local mass m , the metric function \mathcal{A} and the pressure P :

$$m' = \frac{1}{1 - \left(3 + \frac{1}{c_s^2} \right) \tau} \left[\frac{\kappa r^2 \rho}{2} + \xi_p \frac{\bar{X}^p}{\Theta \lambda^2} r^2 - \left(3 + \frac{1}{c_s^2} \right) \frac{\tau}{r} \left(m + \frac{\kappa r^3}{2} (\rho + P) \right) + \frac{\tau}{r} \left(3(r - 2m) + \frac{\kappa r^3 (\rho + P)}{2p} \right) \right], \quad (3.17a)$$

$$\frac{\mathcal{A}'}{2\mathcal{A}} = \frac{1}{(r^2 - 2mr) \left[1 - \left(3 + \frac{1}{c_s^2} \right) \tau \right]} \left[m + \frac{\kappa r^3 P}{2} - \xi_p \frac{\bar{X}^p}{\Theta \lambda^2} r^3 - \tau \left(3(r - 2m) + \frac{\kappa r^3 (\rho + P)}{2p} \right) \right], \quad (3.17b)$$

$$P' = -\frac{(\rho + P)}{(r^2 - 2mr) \left[1 - \left(3 + \frac{1}{c_s^2} \right) \tau \right]} \left[m + \frac{\kappa r^3 P}{2} - \xi_p \frac{\bar{X}^p}{\Theta \lambda^2} r^3 - \tau \left(3(r - 2m) + \frac{\kappa r^3 (\rho + P)}{2p} \right) \right], \quad (3.17c)$$

⁸In GR, the TOV equation reads

$$P' = -\frac{\rho + P}{r(r - 2m)} \left(m + \frac{\kappa}{2} r^3 P \right). \quad (3.13)$$

where τ is given by (3.15), and

$$\Theta = 1 - \frac{(2p-1)r^2}{2p(1-\frac{2m}{r})}\kappa(\rho+P), \quad \bar{X} = \frac{2p(1-\frac{2m}{r}) - (2p-1)r^2\kappa(\rho+P)}{2p\mathcal{A}(1+\frac{r^2}{\lambda^2})}. \quad (3.18)$$

Note that the above equation for P' directly follows from the substitution of (3.17b) into the energy conservation equation (3.3). This is the final system of equations, which we will solve numerically in Section 4.

Before discussing, in the next subsection, a few specific features of the above system, it is worth noting that in the particular case $p = 1/2$, which corresponds to a Horndeski theory, one recovers exactly the same TOV equations as in GR, despite the presence of a non trivial scalar field. Indeed, in this case, the effective energy density ρ_{eff} vanishes since ξ_p , defined in (2.14), and τ , defined in (3.15), are zero. Furthermore, the star's exterior is described by a stealth Schwarzschild metric [21] — the unique Horndeski homogeneous spacetime where the primary hair dependence (2.14) drops out, giving a pure GR geometry with a non trivial scalar (2.12). In summary the “stealth” property for $p = 1/2$ extends from the vacuum solution to the neutron star solution. Since, at the background level at least, the star is identical to its GR counterpart, we will not consider this case further in our discussions.

3.3 Characteristic properties and singularity for the neutron star interior

The star's profile obeys the first order system (3.17a)-(3.17c) which has some special properties as compared to the equivalent system in GR.

Firstly, we note that in the absence of matter ($\rho = P = 0$) all the τ dependent terms in the expression (3.16) for ρ_{eff} drop out, leaving nevertheless the first term which continues to contribute to the equations of motion and in particular to the ADM mass for the vacuum solution (2.17). In other words, the integrated mass $m(R)$ at the surface of the neutron star, where the radius R is defined by $P(R) = 0$, can be different from the ADM mass as measured by an observer at spatial infinity for this class of theories (2.11). This effect, which is of course absent in GR, depends on the sign and magnitude of the scalar charge ξ_p and on the range of λ .

Secondly, we observe that the system (3.17a)-(3.17c) can become become singular if

$$\tilde{\tau} \equiv (3 + \frac{1}{c_s^2})\tau = 1, \quad (3.19)$$

in which case the common denominator on the right-hand side of all three equations vanishes. From (3.15), this is only possible for $\xi_p > 0$, since $\rho + P \geq 0$. For ordinary stars, like the sun, τ is expected to be very small, but for a very compact star, with the metric component \mathcal{A} becoming small, the function $\tilde{\tau}$ can approach, or even reach, unity. Even if τ remains small, the singularity can also occur in a region where the sound speed becomes very low.

A third important point concerns the identical square brackets of (3.17b) and (3.17c) which, unlike the condition (3.19), are independent of the sound speed c_s^2 . Since $\rho + P \geq 0$, in GR the pressure P is always a monotonically decreasing function from the star's center to its surface. For $\xi_p > 0$, however, this behaviour can change dramatically: the pressure may first increase, reaching a local maximum in the star's interior (with \mathcal{A} simultaneously attaining a local minimum at the same point) before eventually decreasing.

For a generic p , such a behavior can be deduced from the radial expansion of the pressure near the star's center (see Appendix A):

$$P = P_c - (P_c + \rho_c) \left[\frac{\kappa}{12} (3P_c + \rho_c) - \frac{\xi_p}{\mathcal{A}_c^p} \left(\frac{2p-1}{4p} \kappa(\rho_c + P_c) + \frac{1}{3\lambda^2} \right) \right] r^2 + \dots \quad (3.20)$$

Whereas the coefficient of r^2 is always negative in GR, it can become positive if the extra term, proportional to $\xi_p > 0$, dominates. The effect becomes more pronounced for larger ξ_p , higher central density ρ_c (and thus smaller \mathcal{A}_c) or smaller λ . Such non-monotonic profiles for the matter pressure and energy density might lead to instabilities under radial perturbations.

Let us go one step further and estimate the influence of the parameters ξ_2 and λ within the squared brackets in the case $p = 2$. Using our definitions (3.8) and (3.15) the modified TOV equation (3.17c) can be written as

$$P' = -\frac{(\rho + P)}{(r^2 - 2mr)(1 - \tilde{\tau})} \left[m + \frac{\kappa r^3 P}{2} \right] + Q, \quad (3.21)$$

where the quantity

$$Q \equiv \frac{(\rho + P)\bar{X}_0}{3r(1 - \tilde{\tau})} \left[\frac{r^2}{\lambda^2} \frac{\Theta^2 - 5\Theta + 10}{1 - \Theta} + 10 - \Theta \right] \tau \quad (3.22)$$

englobes all the beyond GR effects, except the denominator $(1 - \tilde{\tau})$. Assuming here that $\tilde{\tau} < 1$ and $\xi_2 > 0$, we observe that the additional term Q competes with the GR term and can disrupt the monotony of P . Since $\Theta \leq 1$, the term in square brackets in (3.22) is positive and hence small λ or positive large ξ_2 always enhance the magnitude of Q , further modifying the hydrostatic equilibrium relative to GR.

Given the above discussion we expect to find upper bounds in the parameter space spanned by the parameters ξ_2 and ρ_c , as confirmed by our numerical calculations. The precise limits depend on the value of λ and on the equation of state. In Fig. 3.1, we have plotted these boundaries, assuming a polytropic EoS (defined explicitly in the next section), for four different values of the length parameter λ . Note that for higher values of λ , the curves tend to coalesce.

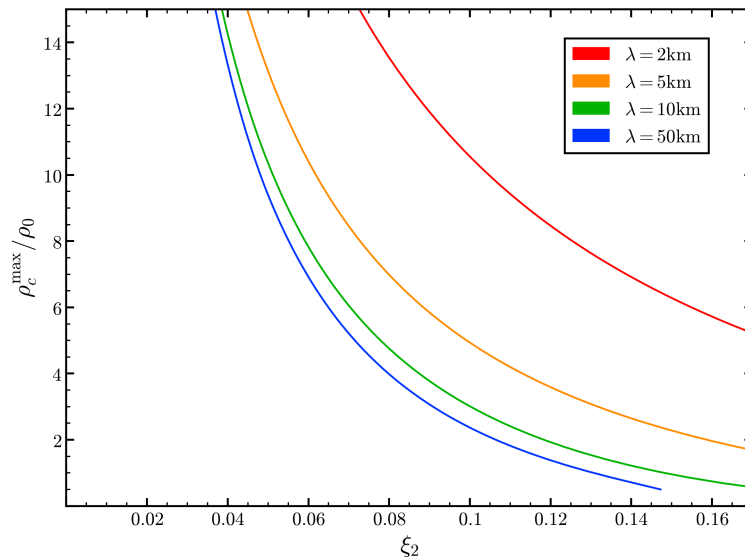


Figure 3.1: Upper bounds in the parameter space (ξ_2, ρ) , defined by the maximal central density ρ_c^{\max} allowed for each ξ_2 , with $\lambda = 2, 5, 10$ and 50 km. The plot corresponds to the polytropic EoS defined in (4.1)-(4.2).

4 Numerical analysis

To understand in more detail how the internal structure of compact stars is affected by the gravitational theories considered here, we integrate numerically equations (3.17a), (3.17b) and (3.17c), supplemented by an EoS. We start with the simple case of a polytropic EoS before progressing to more complex and realistic EoS later on.

4.1 Neutron star structure for a polytropic equation of state

We first consider, for simplicity, a polytropic EoS, which can be written in the following dimensionless form, expressing the pressure and energy density in terms of the particle number density n :

$$\frac{P}{\rho_0 c^2} = K \left(\frac{m_b n}{\rho_0} \right)^\Gamma, \quad \frac{\rho}{\rho_0} = \frac{m_b n}{\rho_0} + \frac{K}{\Gamma - 1} \left(\frac{m_b n}{\rho_0} \right)^\Gamma, \quad (4.1)$$

where $m_b = 1.6749 \times 10^{-24} \text{g}$ is the mean baryonic mass and $\rho_0 = m_b n_0$ ($n_0 = 0.1 \text{fm}^{-3}$ being the typical nuclear number density) is our reference density. In our numerical computations, we have taken the following values for the constant K and the adiabatic index Γ :

$$K = 0.043, \quad \Gamma = 5/3. \quad (4.2)$$

The gravitational theory depends on the value of p , which we choose to be $p = 2$, and the length scale parameter λ , which corresponds to the typical scale on which the scalar interaction is efficient. Finally, the amplitude of the beyond-GR effects is quantified by the parameter ξ_2 , which in principle can vary from one object to another, in contrast to λ . Therefore, once the EoS and the theory are fixed, the neutron star depends on only two parameters: the first one, as in GR, is the central density ρ_c (or n_c), while the second one, ξ_2 , represents in some sense the ‘‘charge’’ of the star.

Given the above EoS and a specific choice of parameters, we compute the radial profiles of the matter and of the metric by integrating Eqs (3.17a), (3.17b) and (3.17c). The integration is performed from the center of the star, where we impose usual regularity conditions, as discussed in Appendix A. The only input is the central energy density ρ_c or, equivalently, the central number density n_c , the central pressure being inferred from the equation of state (4.1). The system is numerically integrated up to the radial point $r = R$ where the pressure vanishes,

$$P(R) = 0, \quad (4.3)$$

thus defining R as the radius of the star. Note that our choice $\Gamma = 5/3$ for the polytropic index prevents the appearance of discontinuities at the surface of the star⁹. The central value of the metric component \mathcal{A} , denoted \mathcal{A}_c , is determined by imposing the boundary condition at spatial infinity $\mathcal{A}(\infty) = 1$.

Fig. 4.1 illustrates how the internal structure of neutron stars is affected by increasing the value of ξ_2 , starting from $\xi_2 = 0$ which corresponds to GR. As ξ_2 increases, one observes that the pressure and energy density in the star’s core decrease less rapidly than in GR, before decreasing much more rapidly in the outer layers of the star. The star radius, indicated by a vertical line, is smaller for higher values of ξ_2 . For the metric component \mathcal{A} , the increase is slower in the star’s core than in GR, but accelerates outward, ultimately exceeding its GR value. The component \mathcal{B} first decreases more sharply than in GR, then rises more rapidly, before joining \mathcal{A} at the surface. We have checked that the numerical integration outside the star reproduces the analytical solution (2.22).

⁹Near the surface of the star, we have $\tilde{\tau} \sim \rho^{2-\Gamma}/(\Gamma K)$ for $\Gamma > 1$. If $\Gamma < 2$, then $\tilde{\tau} \rightarrow 0$, avoiding a discontinuity of the metric and scalar field at the star’s surface (see e.g. [46, 52]).

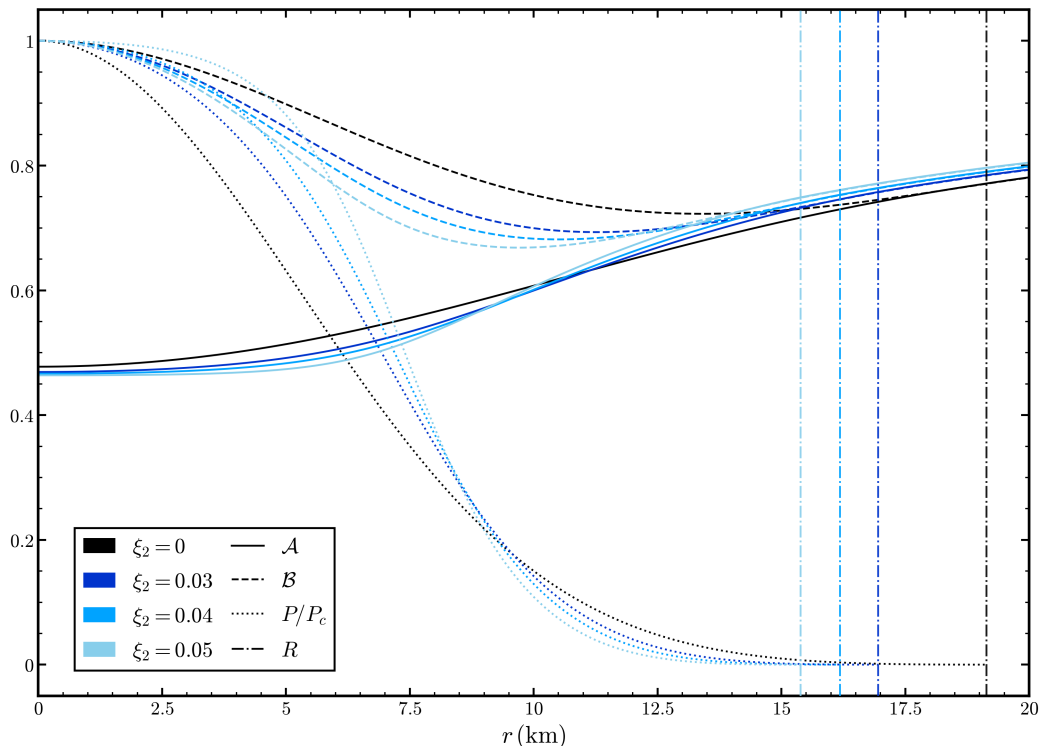


Figure 4.1: Radial profiles of \mathcal{A} , \mathcal{B} and P for the polytropic EoS given by (4.1) and (4.2), assuming $n_c = 4n_0$ and $\lambda = 50$ km. Here we focus on the effect of ξ_2 , plotting the profiles for $\xi_2 = 0$ (GR theory, in black), $\xi_2 = 0.03, 0.04$ and 0.05 (in shades of blue).

As a further exploration, we now study how the length parameter λ affects the neutron star profile. We have plotted in Fig. 4.2 several configurations with the same scalar charge ξ_2 and central density ρ_c , varying λ . A notable feature is that, for sufficiently small λ , stars can exhibit a pressure (and thus matter density) profile that initially increases outward from the center, reaches a maximum, and then decreases in the outer layers. This is in agreement with our comments on the equations of motion made at the end of Section 3.

As shown in Fig. 4.3 — and consistent with Eq. (3.20) — the specific features discussed above are more pronounced for larger ξ_p , higher central density (i.e. more relativistic stars), or smaller λ . Indeed, as shown in the top panels, it is easier to find a “pressure peak”, instead of a monotonic pressure, for smaller λ or larger ξ_p . The radius corresponding to the maximum of the pressure also tends to be closer to the center of the star when the amplitude of the peak increases, as illustrated by the last figure at the bottom. One also notes that the metric component \mathcal{A} decreases in the central region, again in contrast with the usual GR behaviour, but in accordance with the standard conservation equation (3.3) since P increases.

It is also instructive to examine the radial profile of the effective energy density ρ_{eff} inside the star. In Fig. 4.4, we plot ρ_{eff} , ρ and the local mass m for three configurations corresponding to those of Fig. 4.2. For small λ , ρ_{eff} increases significantly in the star’s core, which can be understood from Eq. (A.9). In the outer layers, however, this trend reverses, with ρ_{eff} even becoming slightly negative near the surface. This sign change is explained by Eq. (3.9): the term \bar{X}'/\bar{X} is negative in the core (see the right panel of Fig. 4.4, where \bar{X} is plotted) and dominates the first term, yielding $\rho_{\text{eff}} > 0$. This is no longer the case in the outer layers, which explains why ρ_{eff} becomes negative.

We also observe that, for small values of λ , typically well below the star radius, the local mass m

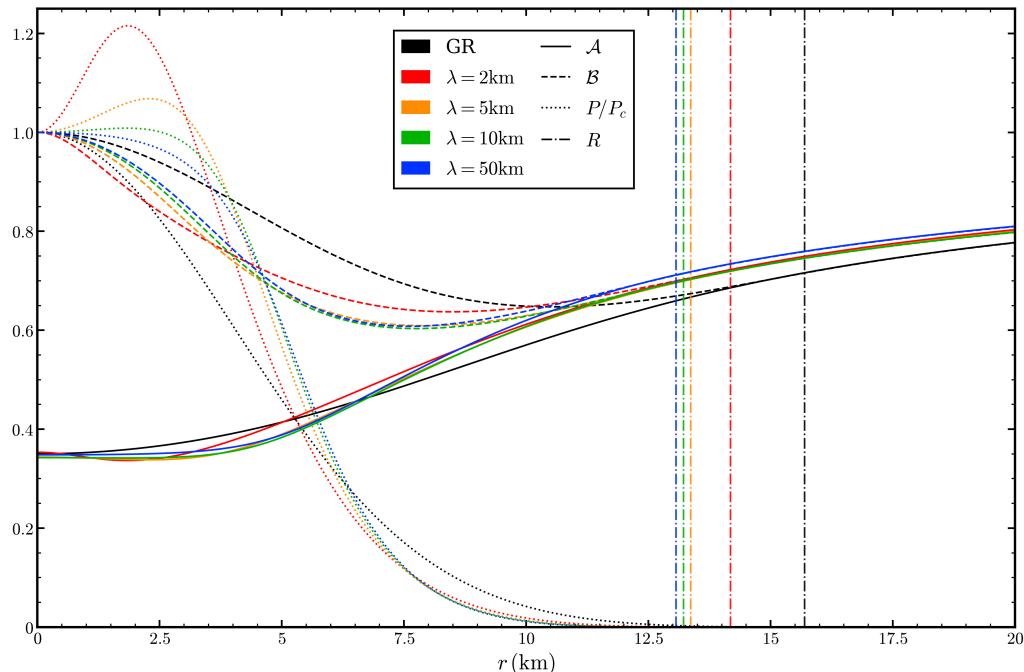


Figure 4.2: Radial profiles of \mathcal{A} , \mathcal{B} and P for the polytropic EoS, assuming $n_c = 8n_0$ and $\xi_2 = 0.03$. Here we focus on the effect of λ , plotting the profiles for $\lambda = 2, 5, 10$ and 50 km. These are to be compared with the GR case pictured in black.

has the same typical radial evolution as in GR. Indeed, for $\lambda = 5$ km in the figure, the mass increases within the star and settles to its ADM mass value at the surface. For higher values of λ ($\lambda = 10$ or 50 km in the figure), however, although the mass m is nearly constant near the surface, it starts to grow again outside the star, only approaching its ADM value M at larger distances. This difference in behavior arises from the influence of the scalar field in the exterior region, whose range increases with λ (see Eq.(3.18)). Moreover, for larger values of λ , M becomes larger than in GR. At intermediate radii in the exterior region, the effective mass $m(r)$ depends on the position of the observer.

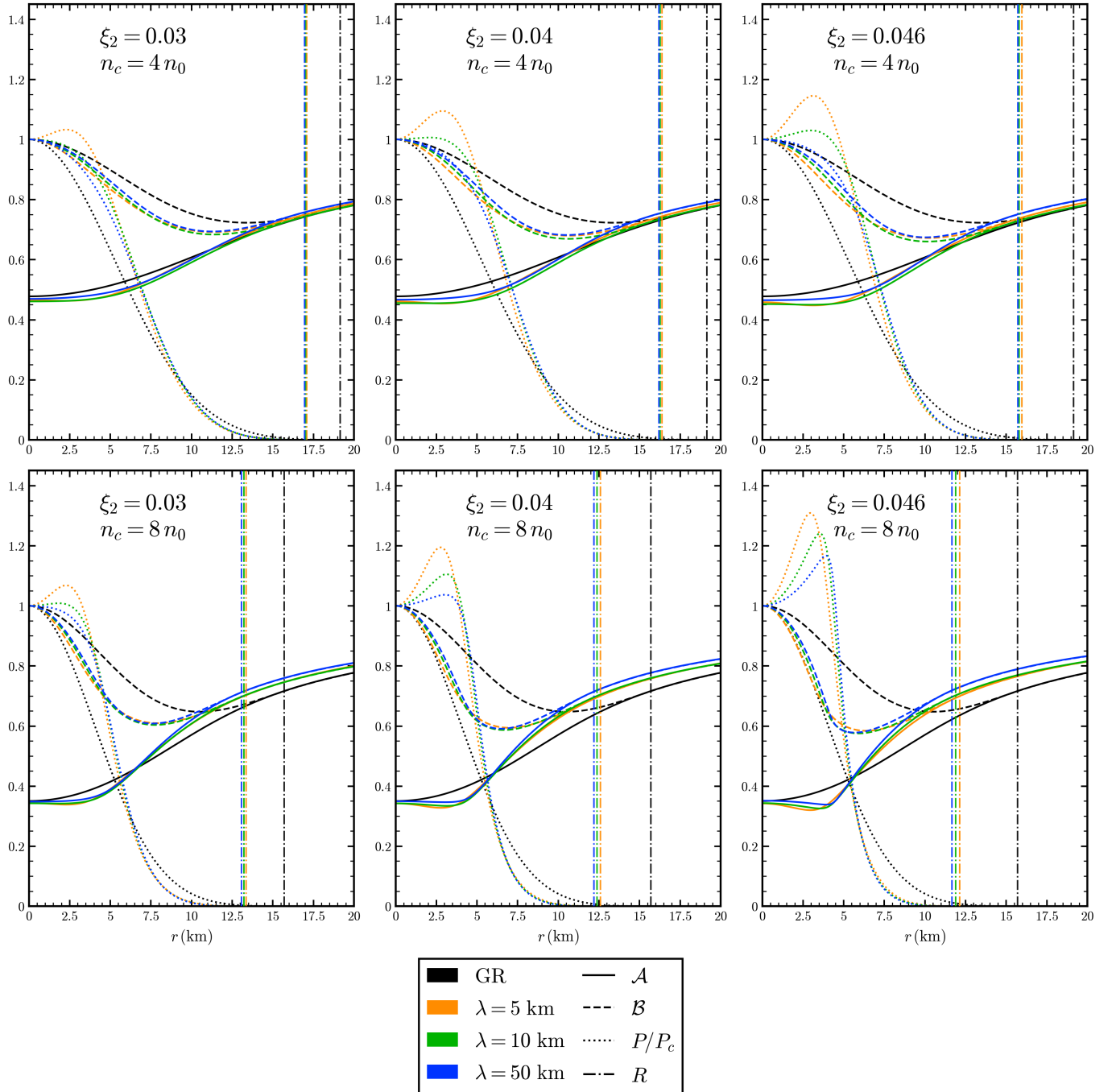


Figure 4.3: Radial profiles of \mathcal{A} , \mathcal{B} and P for the central densities $n_c = 4 n_0$ (top) and $n_c = 8 n_0$ (bottom), using the polytropic EoS. Here, we study the combined effect of λ and ξ_2 , for $\lambda = 5, 10$ and 50 km; from left to right, ξ_2 is taken to be $0.03, 0.04$ and 0.046 (close to the critical value 0.047 where the singularity appears).

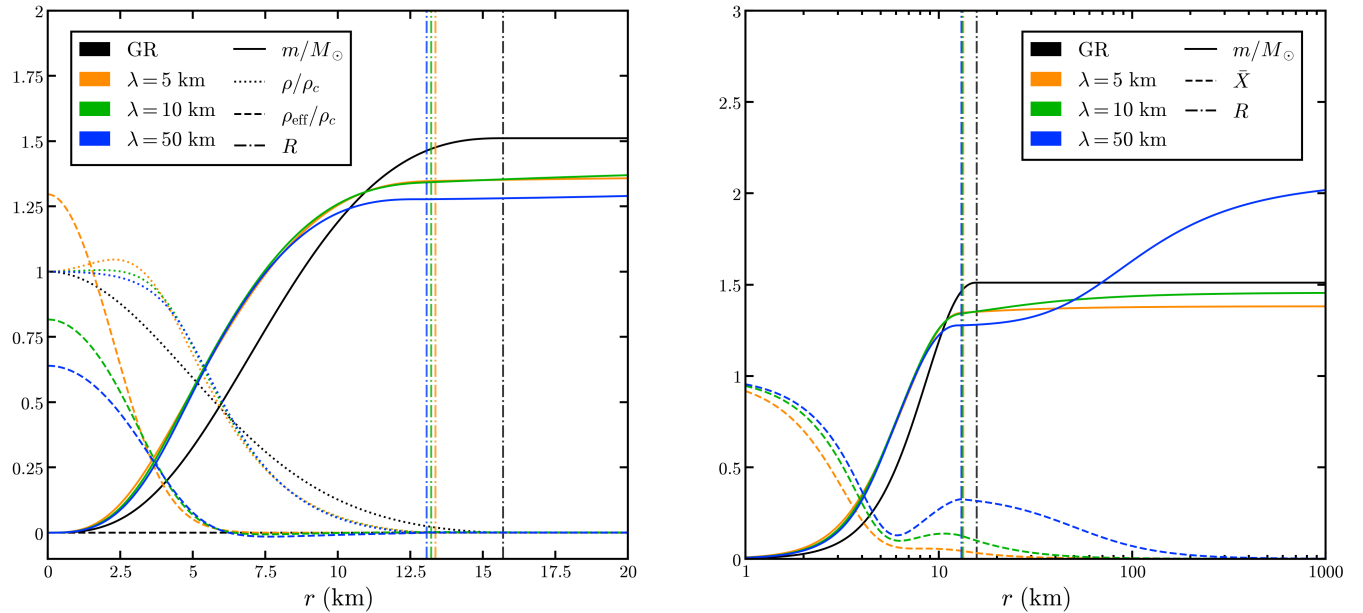


Figure 4.4: Radial profiles of m , ρ , ρ_{eff} and \bar{X} for $\lambda = 5, 10$ and 50 km, with the polytropic EoS, $n_c = 8n_0$ and $\xi_2 = 0.03$. The left panel shows the profile of m , ρ and ρ_{eff} within the star, while the right one focuses on the behavior of m and \bar{X} at larger distances. Note that for $\lambda = 50$ km (blue curve), m continues to increase beyond the star's surface until it reaches its ADM value far away.

4.2 Phenomenological equations of state

We now consider three more complex EoS commonly used in neutron star studies: SLy, BSk21 and BSk22. As discussed in [63, 64], these EoS can be conveniently parametrized in the form

$$\begin{aligned} \log_{10} \left(\frac{P/c^2}{\text{g} \cdot \text{cm}^{-3}} \right) &= \frac{b_1 + b_2\chi + b_3\chi^3}{1 + b_4\chi} U[b_5(\chi - b_6)] \\ &+ (b_7 + b_8\chi) U[b_9(b_{10} - \chi)] + (b_{11} + b_{12}\chi) U[b_{13}(b_{14} - \chi)] \\ &+ (b_{15} + b_{16}\chi) U[b_{17}(b_{18} - \chi)] + \frac{b_{19}}{b_{20}^2(b_{21} - \chi)^2 + 1} + \frac{b_{22}}{b_{23}^2(b_{24} - \chi)^2 + 1} \end{aligned} \quad (4.4)$$

with

$$U[x] \equiv \frac{1}{e^x + 1}, \quad \chi = \log_{10}(\rho/(\text{g} \cdot \text{cm}^{-3})). \quad (4.5)$$

Each EoS corresponds to different values of the coefficients b_i . The 18 coefficients for the SLy equation of state¹⁰ are given in the left table of App. B, based on [63], while the 24 coefficients for BSk21 and BSk22 are listed in the right table of App. B, based on [64, 65]. All three EoS are represented in Fig. 4.5, along with the polytropic EoS (4.1).

In Fig. 4.6 we have plotted the profile of a neutron star with the SLy equation of state for several values of ξ_2 , fixing λ to 5 km and the central density to $\rho_c = 4\rho_0$. This figure should be compared with some of the configurations plotted in Fig. 4.3. One notes that the pressure profile is monotonic for the lowest (non GR) value of ξ_2 but exhibits a maximum at an intermediate radius for the highest values of ξ_2 .

¹⁰The coefficients b_i for $19 \leq i \leq 24$ vanish in this case.

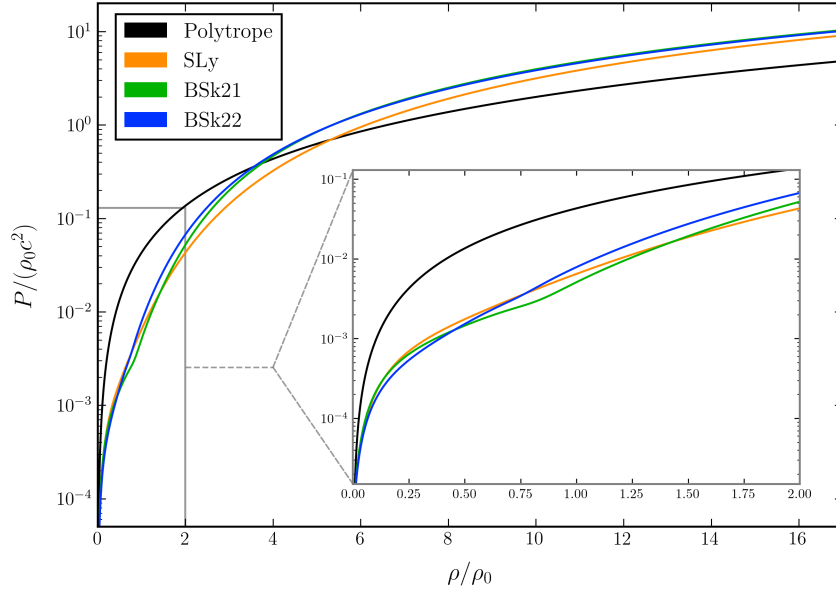


Figure 4.5: Polytropic, SLy, BSk21 and BSk21 EoS, plotted for $\rho \leq 17\rho_0$. The frame zooms in on the curves in the range $[0, 2\rho_0]$.

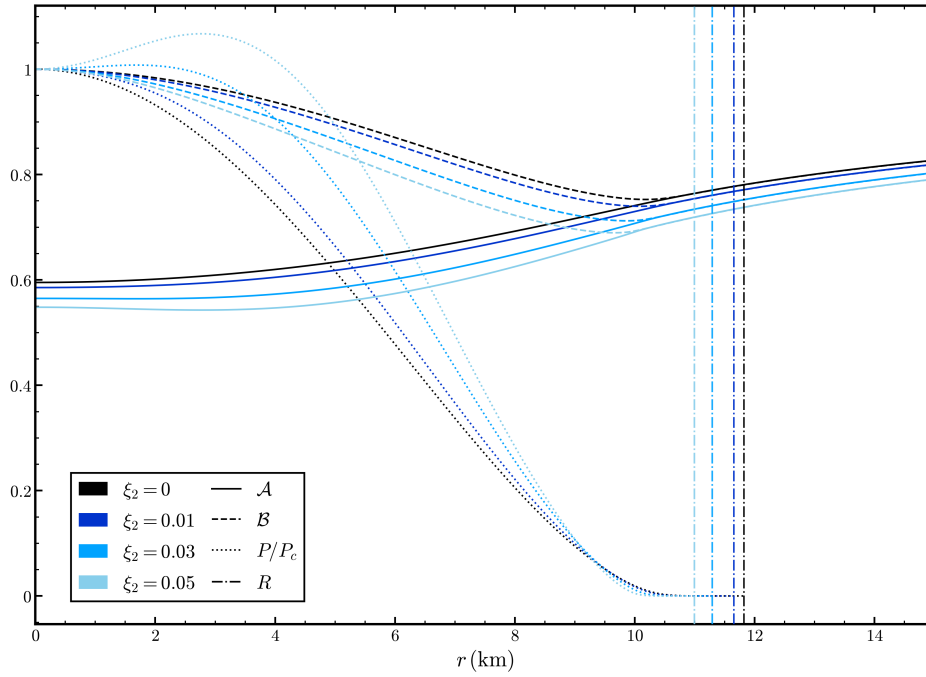


Figure 4.6: Radial profiles of \mathcal{A} , \mathcal{B} and P for $\xi_2 = 0.01, 0.03$ and 0.05 (in shades of blue), with the SLy EoS, $\rho_c = 4\rho_0$ and $\lambda = 5$ km. As before, the GR profile is in black.

As we stressed in Subsection 3.3, the differential system governing the radial profile of a relativistic star breaks down when the quantity $\tilde{\tau}$, defined in (3.19), reaches the value 1. This condition can be fulfilled either if τ is large enough or if c_s becomes small enough. This is illustrated in Fig. 4.7, for the SLy EoS, with two distinct values of ξ_2 and of ρ_c , both near the critical limit associated with a singular

system. For the higher value of ξ_2 (red curves), there is a single peak for $\tilde{\tau}$, almost reaching 1, due to a very small value of c_s . By contrast, for the smaller value of ξ_2 (blue curves), one observes two peaks: the higher peak corresponds to a large value of τ , whereas the slightly lower peak is associated with a suppressed c_s . In such cases, a slight change of the central density can abruptly shift the singularity from one caused by a large τ to one arising from a small c_s . This explains the sudden slope changes observed in Fig. 4.8, in contrast to Fig. 3.1 (where c_s never becomes small enough). The precise value where this transition occurs depends on the equation of state and on λ .

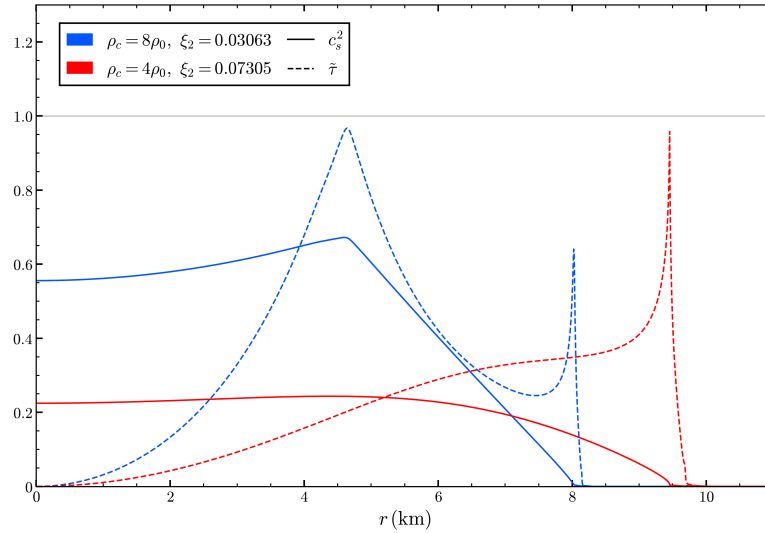


Figure 4.7: Radial profiles of c_s^2 and τ for two almost singular configurations. We are using the SLy EoS and $\lambda = 10$ km.

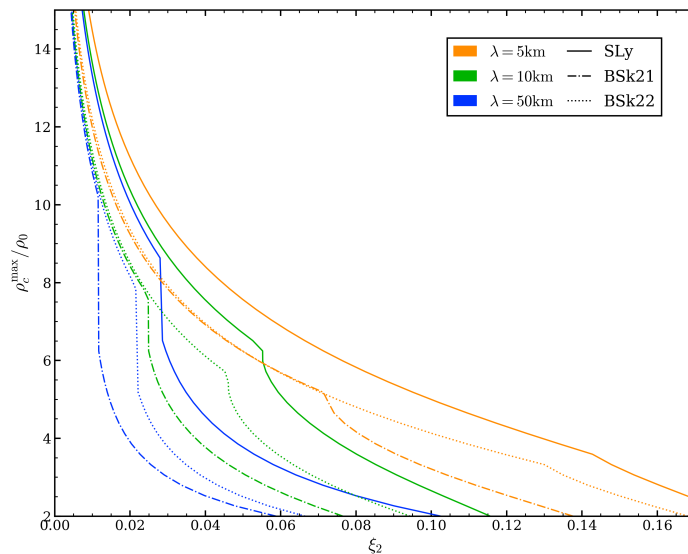


Figure 4.8: Maximal central density ρ_c^{\max} allowed for each ξ_2 and for $\lambda = 2, 5, 10$ and 50 km, in the case of the SLy EoS.

The sign of X outside the star is positive by construction, since the gradient of the scalar field is

time-like. For most configurations, X is also positive throughout the star. However, in some cases the integration of the differential system from the center of the star yields a negative value of X for some intermediate range of the radial coordinate, as illustrated in Fig. 4.9. This boils down to a change in the sign of Θ in (3.8) which in turn depends on the matter back-reaction on the scalar kinetic term X . This is a very intriguing feature as it means that the gradient of the scalar field — always time-like in the star’s core (see Eq. (A.7))— can become space-like in an intermediate region before reverting to time-like in the outer layers and exterior. We stress that the differential system remains regular as X crosses zero. However, it is natural to wonder whether this sign flip could trigger physical instabilities. This would require analyzing the linear perturbations around such a sign-flipping configuration.

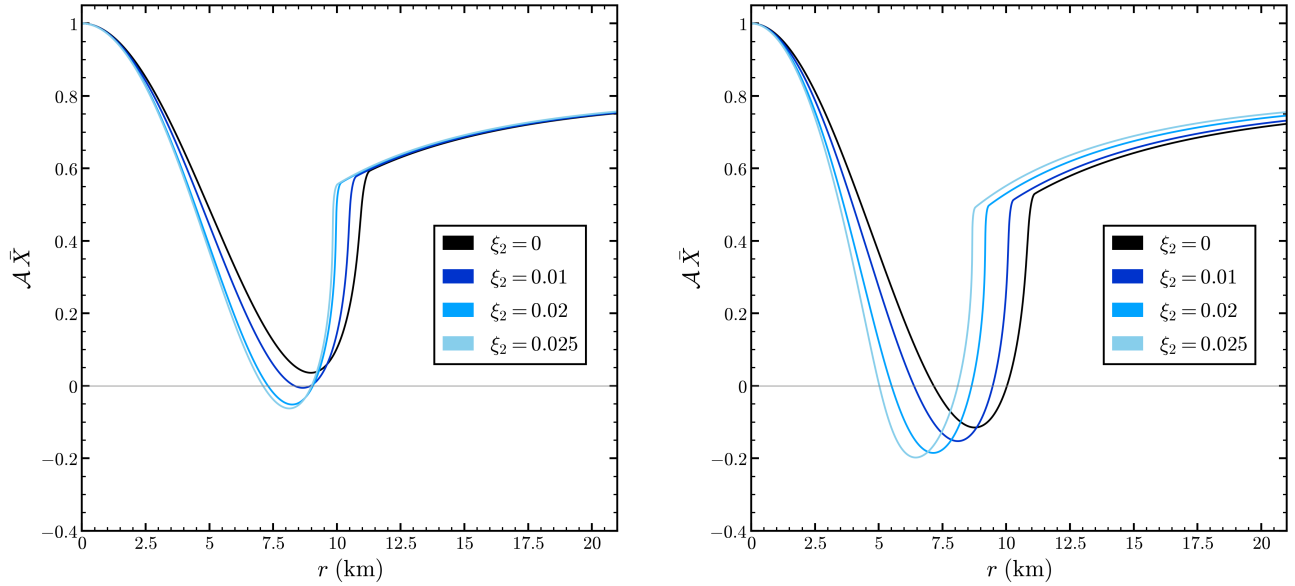


Figure 4.9: Radial profile of $\mathcal{A}\bar{X}$ showing the possible change of sign of the scalar density X in the star interior. Here we consider the SLy equation of state, two central densities, $\rho_c = 6.5\rho_0$ (left panel) and $\rho_c = 8\rho_0$ (right panel), $\lambda = 50$ km and $\xi_2 = 0, 0.01, 0.02$ and 0.025 .

4.3 Mass-radius relation

As noticed in the various star configurations shown earlier, the star’s radius in modified gravity differs from that of a GR star with the same central density. The mass of the star is also affected. To discuss how the latter depends on the various parameters, it is instructive to go back to the exact exterior solution (2.13). The constant μ that appears in this equation can be determined numerically from the metric component of the internal solution evaluated at the star radius R :

$$\mu = \frac{R}{2} [1 - \mathcal{A}(R)] - \xi_p \lambda \Xi_p(R/\lambda). \quad (4.6)$$

According to (2.17), the ADM mass is then given by

$$M \equiv \frac{R}{2} [1 - \mathcal{A}(R)] + \xi_p \lambda \left[\frac{\sqrt{\pi} \Gamma(p - \frac{3}{2})}{4 \Gamma(p)} - \Xi_p(R/\lambda) \right], \quad (4.7)$$

which, in the particular case $p = 2$, reduces to

$$M \equiv \frac{R}{2} [1 - \mathcal{A}(R)] + \frac{1}{2} \xi_2 \lambda \left[\arctan(\lambda/R) + \frac{R/\lambda}{1 + (R/\lambda)^2} \right]. \quad (4.8)$$

If the star radius is much larger than λ , the term proportional to ξ_2 becomes negligible and the mass is given by

$$M \simeq \frac{R}{2} [1 - \mathcal{A}(R)] \quad \text{for } R \gg \lambda, \quad (4.9)$$

whereas, in the opposite limit, we find

$$M \simeq \frac{R}{2} [1 - \mathcal{A}(R)] + \frac{\pi}{4} \xi_2 \lambda \quad \text{for } R \ll \lambda. \quad (4.10)$$

This latter expression applies to the case $\lambda = 50$ km plotted in Fig. 4.4. Moreover, if $R \ll \xi_2 \lambda$, one even finds that the ADM mass, measured at spatial infinity, is essentially given by the second term, i.e. $M \simeq \pi \xi_2 \lambda / 4$. Note, however, that observers situated at a sufficiently small distance from the star will measure a mass that differs from the ADM mass.

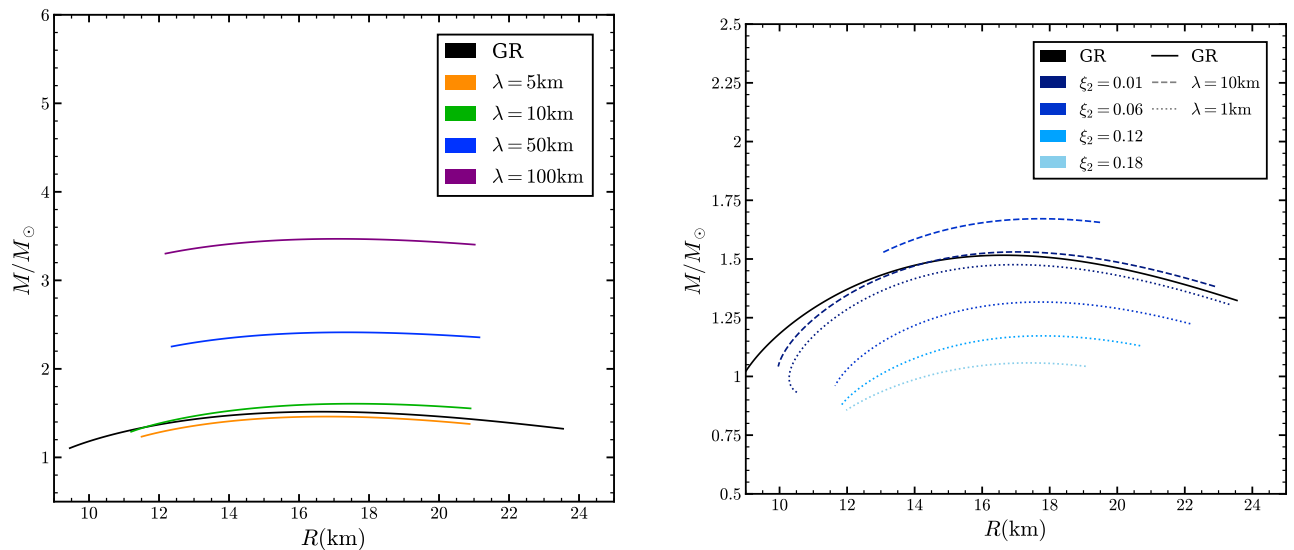


Figure 4.10: Mass-radius relation $M(R)$ for compact stars with the polytropic EoS (with $\rho_c \geq 2\rho_0$). The left panel focuses on the influence of the theory-fixed parameter λ , for $\lambda = 5, 10, 50$ and 100 km, with $\xi_2 = 0.04$. The right panel focuses on the influence of the star-dependent parameter ξ_2 , showing the cases $\xi_2 = 0.01, 0.06, 0.12$, for the theory parametrised by $\lambda = 10$ km.

By varying the central density, we can compute many neutron star configurations and thus determine the mass-radius relation, depending on the equation of state and on the modified gravity parameters. In Fig. 4.10, we plot this mass-radius relation in the case of our polytropic EoS. The GR case, corresponding to $\xi_2 = 0$, is plotted as a solid black curve. Overall, the mass-radius relations exhibit the usual shape expected for equilibrium compact stars: as the central density is increased, the mass increases, reaches a maximum, and then decreases, corresponding to the threshold of dynamical instability, as determined by the condition $dM/d\rho_c = 0$. The colored curves associated with different values of λ or ξ_2 show that this qualitative behavior is preserved, but the curves are shifted relative to GR. In particular, the left panel shows how the mass-radius relation is affected by the variation of λ , while ξ_2 remains fixed. One observes that for a given radius, the mass tends to decrease, with respect to GR (black curve), for small values of λ . By contrast, it increases for large values of λ . This observation can be explained by the two limiting expressions obtained above. When λ becomes large, the mass is dominated by the second term in (4.10), which is proportional to $\xi_2 \lambda$. By contrast, for a small λ , we find that the mass is smaller, at fixed radius. The right panel shows how this mass-radius

relation changes when ξ_2 varies. Essentially, as ξ_2 increases, the corresponding curve is further away from the GR curve, in either direction depending on the value of λ . Let us note that the curves stop on the left hand side when the maximal central density is reached. On the right hand side of the curve (see for instance the right panel), the limit corresponds to the minimum central density explored numerically, here $\rho_c = 2\rho_0$.

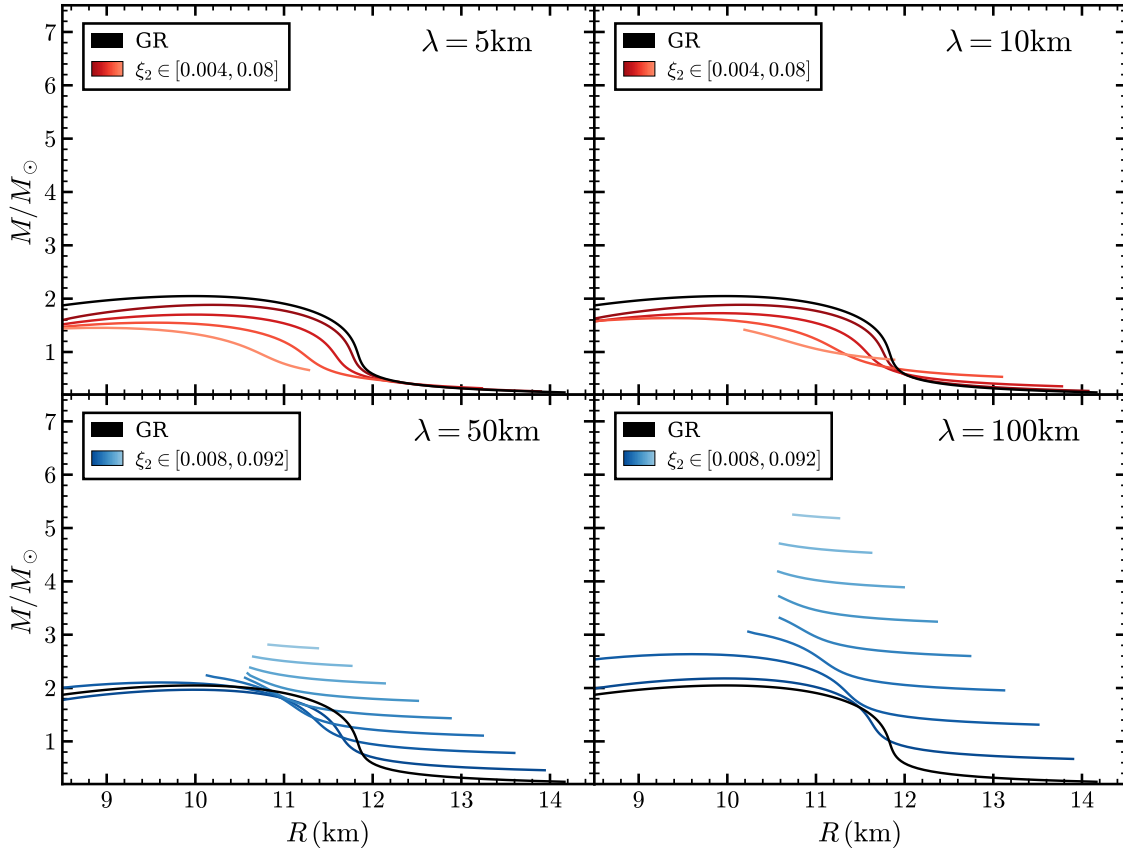


Figure 4.11: Mass-radius relation $M(R)$ for the SLy EoS. In the top panels we consider $\lambda = 5$ and 10 km respectively for values $\xi_2 = 0.004, 0.016, 0.04$ and 0.08 . We notice that for small values of λ the mass range (in shades of red) is relatively independent of the value of ξ_2 . For the bottom panels however (considering the larger values $\lambda = 50$ and 100 km), the mass range (in shades of blue) differs significantly depending on ξ_2 , taken here in the array starting from 0.008 up to 0.092 , with an increment of 0.012 . The curves stop on the left when they reach the maximum central density to avoid a singularity and, on the right, for the minimal central density $\rho_c = 2\rho_0$ considered in our computations.

Similar plots of the mass-radius relation can be drawn for more realistic equations of state, for example SLy in Fig. 4.11. Again, the mass-radius curve is shifted to smaller masses when λ is smaller than the star's radius, whereas for large λ , the second term in (4.10) becomes more and more prominent. For this reason, it is instructive to plot the relation between the radius and the mass μ , which is independent of the extra term proportional to λ . In Fig. 4.12, one clearly sees that the intrinsic mass μ is reduced with respect to the mass of a GR star with the same radius. We also note that, for realistic equations of state, the mass μ is more sensitive to the parameter ξ_2 than for polytropic equations of state (compare the increment of ξ_2 in the left and right plots of Fig. 4.10). This can be related to the

property that realistic EoS have a higher adiabatic index at high density, which enhances the impact of the modified gravity effects on the star profile.

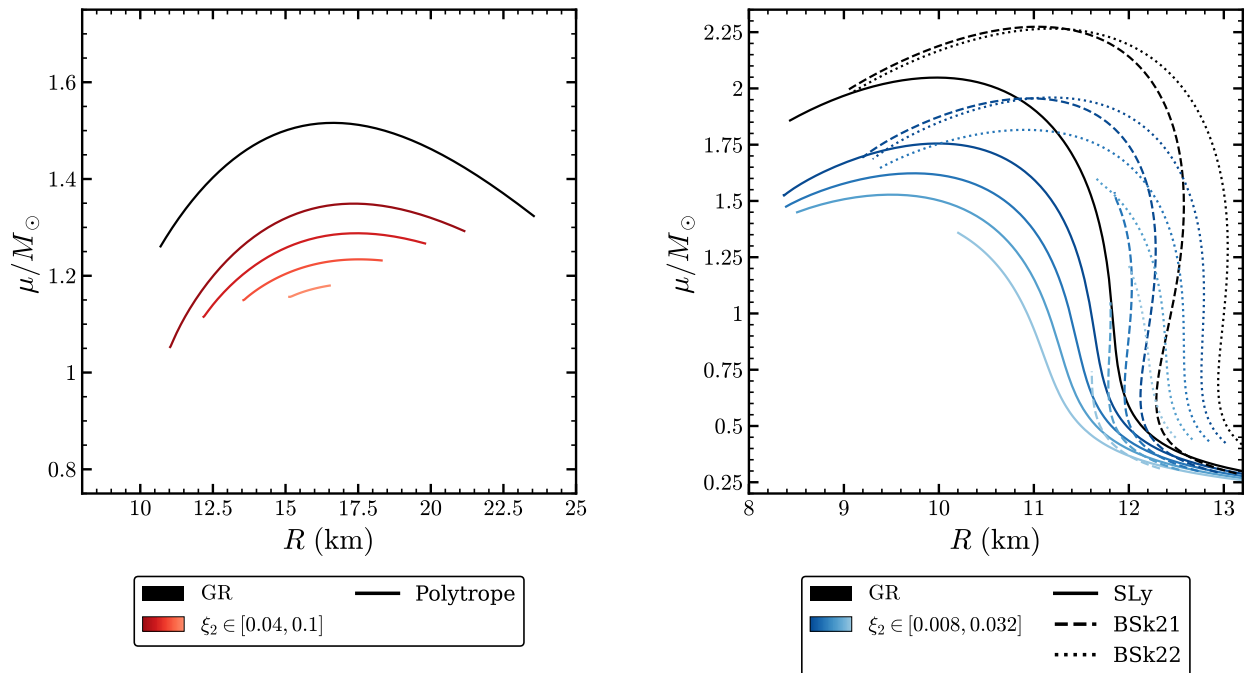


Figure 4.12: Relation $\mu(R)$ for $\lambda = 50$ km, for all EoS studied. The left plot corresponds to the polytropic EoS, for ξ_2 from 0.04 to 0.10 with an increment of 0.02. The right plot corresponds to the SLy, BSk21 and BSk22 EoS, for ξ_2 from 0.008 to 0.032 with an increment of 0.008.

4.4 Case of negative scalar charge

We now discuss briefly the cases where the coupling parameter ξ_p takes negative values, which appears to lead to puzzling — and likely problematic — consequences. For $\xi_p < 0$, the effective energy density ρ_{eff} is now negative in the innermost part of the star, and positive near the surface (because the dominant term \bar{X}'/\bar{X} in Eq.(3.9) becomes positive near the surface, as shown in Fig. 4.13, while the effective pressure is positive, acting against the gravitational pull in addition to the ordinary pressure. Therefore, neutron stars now tend to be less compact, leading to larger radii for a given mass. This behavior can be observed in the mass–radius diagram of Fig. 4.14, showing a larger radius compared to the GR prediction.

A surprising consequence of a negative effective energy density is that the ADM mass can become negative. Indeed, by integrating (3.11), one finds

$$M = M_m + M_{\text{eff}} \quad (4.11)$$

with

$$M_m = 4\pi \int_0^R \rho r^2 dr, \quad M_{\text{eff}} = M_{\text{eff}}^{\text{in}} + M_{\text{eff}}^{\text{out}} \equiv 4\pi \int_0^R \rho_{\text{eff}} r^2 dr + 4\pi \int_R^\infty \rho_{\text{eff}} r^2 dr, \quad (4.12)$$

where we have distinguished the interior and exterior effective mass contributions¹¹.

¹¹One can even find cases where $|M_{\text{eff}}^{\text{in}}| > M_m$, for low values of λ and ρ_c , along with a sufficiently high value of $|\xi_2|$.

The matter contribution to the mass, M_m , is of course positive, but the interior effective mass $M_{\text{eff}}^{\text{in}}$ is negative. Moreover, the external effective mass is given by

$$M_{\text{eff}}^{\text{out}} = \xi_p \left[\frac{\sqrt{\pi} \Gamma(p - \frac{3}{2})}{4 \Gamma(p)} - \Xi_p(R/\lambda) \right] \lambda, \quad (4.13)$$

where the term in the brackets is always positive. Thus $M_{\text{eff}}^{\text{out}}$ is also negative for negative ξ_p and, when $\lambda \gg R$, becomes proportional to λ :

$$M_{\text{eff}}^{\text{out}} \simeq \xi_p \frac{\sqrt{\pi} \Gamma(p - \frac{3}{2})}{4 \Gamma(p)} \lambda \quad \text{for } \lambda \gg R. \quad (4.14)$$

It is thus possible to obtain stars with arbitrarily large negative mass by increasing λ . This can be seen in Fig. 4.14, for $\lambda = 50$ km and $\lambda = 100$ km, with small central energy density.

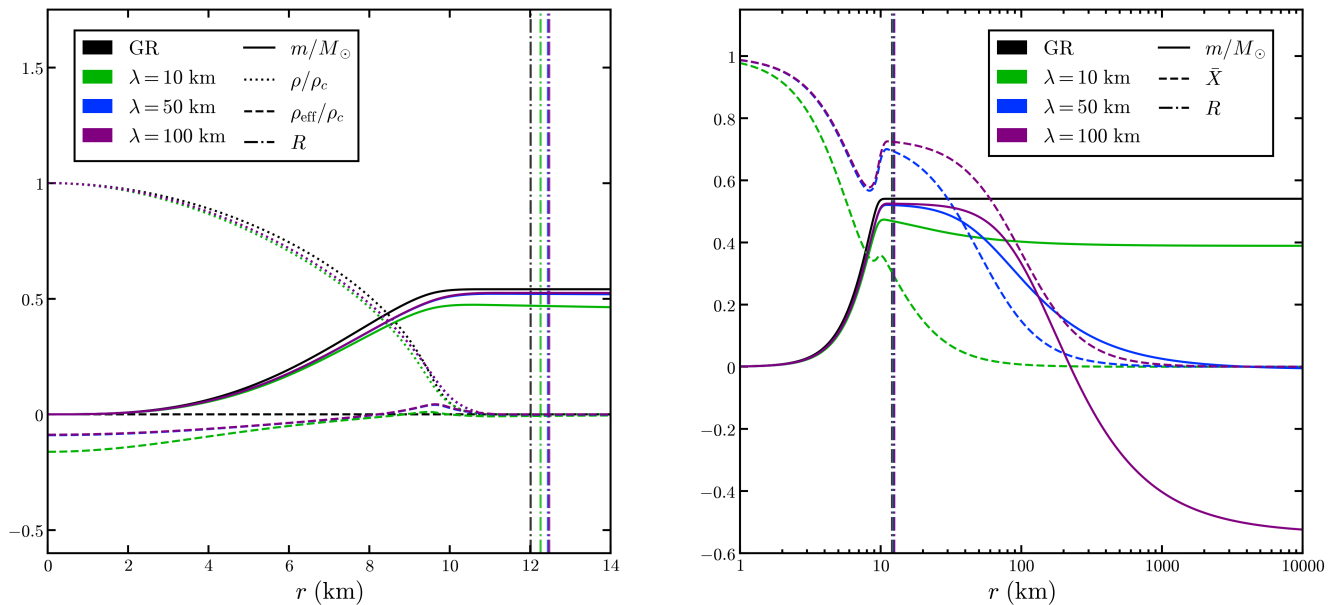


Figure 4.13: Radial profiles of m , ρ , ρ_{eff} and \bar{X} for the SLy EoS, for $\lambda = 10, 50$ and 100 km, $\rho_c = 3\rho_0$ and $\xi_2 = -0.02$. The left plot gives the profile of m , ρ and ρ_{eff} within the star, while the right one focuses on the behavior of m and \bar{X} at larger distances. Note that for $\lambda = 100$ km (purple curve), m eventually becomes negative.

At very high central densities, the star exhibits unusual behaviour: both its mass and radius increase with ρ_c . Indeed, as ρ_c rises, the effective energy density in the core becomes increasingly negative, while the effective pressure grows simultaneously. This causes ordinary matter to rarefy in the core and accumulate in the outer layers. The additional pressure from the effective fluid both supports a higher mass and, through its repulsive effect, increases the radius.

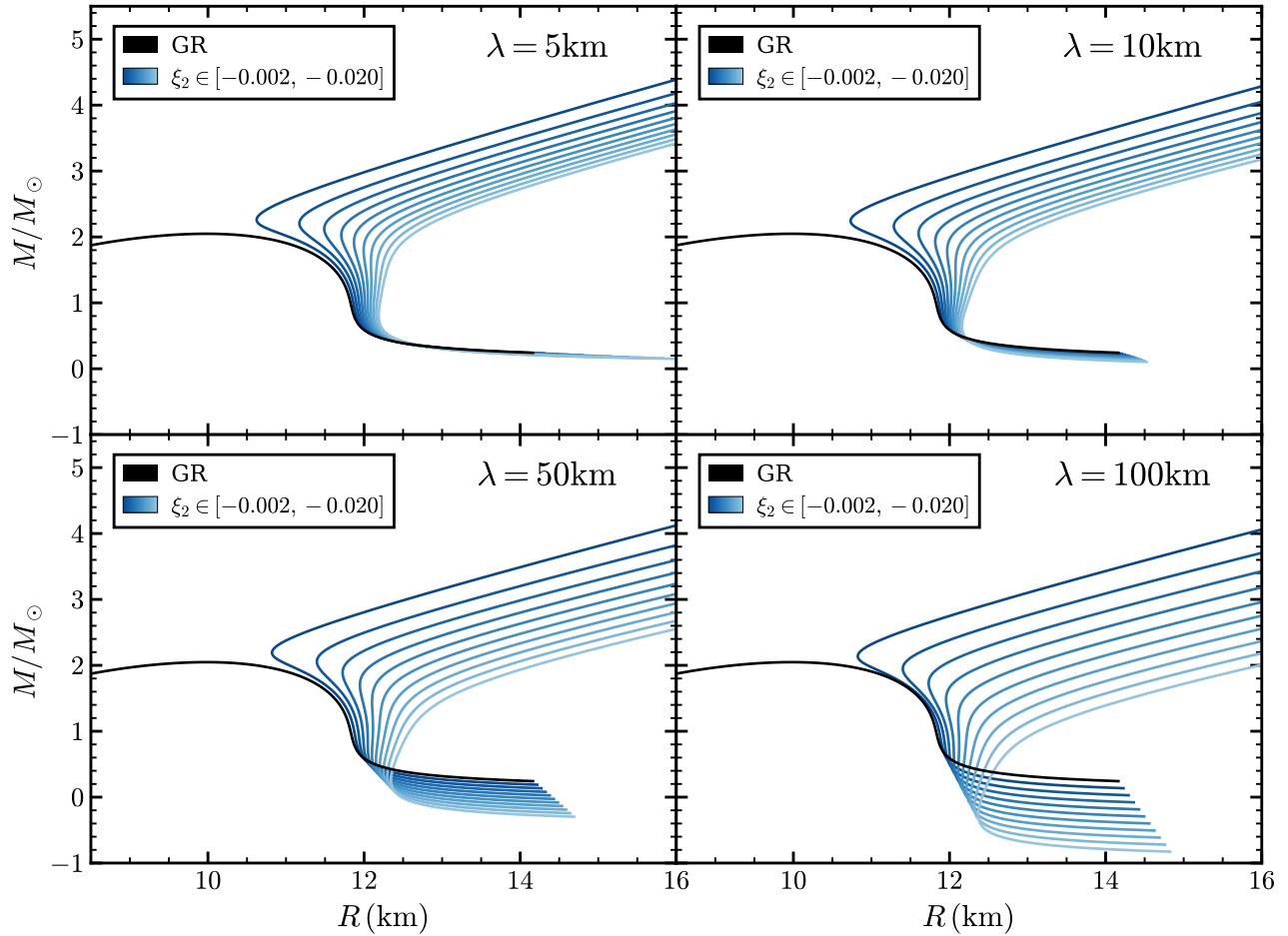


Figure 4.14: Mass-radius relation $M(R)$ for the SLy EoS in the case of a negative scalar charge, for $\lambda = 5, 10, 50$ and 100 km and ξ_2 varying from -0.002 to -0.020 with an increment of 0.002 .

5 Conclusions

We have constructed neutron star solutions within a subfamily of DHOST theories, exploiting their global shift and parity symmetries. These theories are parametrised by two coupling constants and a positive exponent p , which we fixed to 2 to obtain a simple closed-form solution for the vacuum spacetime.

As in GR, the neutron star interior is modeled as a perfect fluid, with the solution matching an exact vacuum solution at the star's surface. Unlike previous solutions in DHOST theories, the neutron stars we have constructed carry a finite scalar charge ξ_p (defined in Eq. (2.14)), which acts as a free parameter, analogous to the mass or electric/magnetic charge in GR. In addition, the solutions depend on a characteristic length scale λ — fixed by the theory — which sets the range of the scalar field's effects on the geometry. The exterior solution corresponds to the black holes with primary scalar hair recently discovered in [21] and further extended in the literature (see for example [23], [22], [36]).

For sufficiently high values of ξ_p , the neutron star solutions we obtained exhibit striking features that depart significantly from their GR counterparts (with the same central energy density and equation of state). The origin of these differences can be traced back to the scalar field kinetic term, which now depends on the matter (see Eq. (3.8)) and can drastically change what happens in the interior of the

compact object by a cascading effect in the field equations.¹² As a result, the matter energy density (and pressure) can increase when going outwards in the star’s core, in contrast with the usual GR behaviour. One may suspect that this feature is associated with instabilities¹³ and deserves further investigation, particularly of radial perturbations, which we plan to do study in future work. Furthermore, we have found that, at a finite distance inside the star, a singularity of the field equations may appear for a sufficiently large (positive) scalar ξ_p or a small λ , when the central density is high. Another surprising property of the configurations we have obtained is the possibility for the scalar field gradient to evolve from time-like at the star’s center to space-like inside an intermediate region of the star to time-like again near the surface and outside.

As mentioned earlier, an interesting property of our system is the very particular back-reaction of matter on the scalar field kinetic term X , as depicted by Eq. (3.8) in the star’s interior. Reciprocally, the impact of the scalar field on the star profile is embodied in the radially-dependent effective energy density ρ_{eff} and pressure P_{eff} , with equation of state $P_{\text{eff}} = -\rho_{\text{eff}}$. Interestingly, a jump in the energy density and pressure due to a phase transition inside the neutron star (see for example [68]) would have no direct impact on the quantities Θ , defined in (3.8), and τ , defined in (3.15), that characterise the beyond-GR effects since they depend on the combination $\rho + P$.

Quite recently, black holes with primary hair were found [69–71] within a generic class of vector-tensor theories (see for example [72]). These acquired a quite distinct construction from that used in [21] which is interestingly related to a Weyl rather than Levi-Civita connection in higher dimensional Lovelock theory [73, 74]. It was found [71] that one can have an arbitrarily small cosmological constant as primary hair. It would be worthwhile to investigate the effects of such a parameter on compact objects, like neutron stars, within these theories and see what it may entail in terms of observations.

We have seen that, *outside* a compact object, the scalar field interferes in the local versus far-away gravitational pull of the object, with respect to standard GR. It would be interesting to study whether there exists some astrophysical system where such an effect could yield valuable constraints on λ and ξ_p .

To determine whether the strange behaviours we have observed — at least for some values of the parameters — such as the $X = 0$ crossing, the non-monotonic matter profile, are physically relevant, it would be crucial to consider linear perturbations of our stars. This would presumably show that some configurations are unstable, thereby imposing more stringent constraints on our beyond-GR parameters.

Another interesting direction would be to extend our study to solutions associated with non-homogeneous exterior metrics, obtained via disformal transformations of the neutron star solutions at hand. In particular, it would be valuable to investigate whether the matter singularities observed here could be alleviated under certain of disformal deformations.

Acknowledgements

HB would like to sincerely thank both laboratories *Astroparticule et Cosmologie* (APC) and *Laboratoire de Physique des 2 Infinis Irène Joliot Curie* (IJCLab) for hosting him during the initiation of this work. CC would like to thank fruitful discussions with George Pappas during his visits in the Observatory of the University of Thessaloniki.

¹²Note that although the scalar field is not directly coupled to matter, it is the nonlinear nature of the modified TOV equations that lead to these backreaction effects in the star’s interior.

¹³It has been noted that some matter instabilities may emerge in certain classes of DHOST theories (see for example [66, 67]).

A Expansion near the center of the equations of motion

In this appendix, we present the behavior of the functions \mathcal{A} , \mathcal{B} and P near the center of the star. Regularity at the center imposes the boundary conditions are $\mathcal{A}'(0) = \mathcal{B}'(0) = P'(0) = 0$ and $\mathcal{B}(0) = 1$, which leads to the following expansions near $r = 0$:

$$\mathcal{A}(r) = \mathcal{A}_c + \mathcal{A}_2 r^2 + \dots \quad (\text{A.1})$$

$$\mathcal{B}(r) = 1 + \mathcal{B}_2 r^2 + \dots \quad (\text{A.2})$$

$$P(r) = P_c + P_2 r^2 + \dots, \quad (\text{A.3})$$

where \mathcal{A}_2 , \mathcal{B}_2 and P_2 are constants. To determine these constants in terms of ρ_c and P_c , we substitute the above expressions into the background equations (3.4a), (3.4b) and (3.3) and obtain

$$\mathcal{B} = 1 - \left(\frac{\kappa}{3} \rho_c + \frac{\xi_p(2p-1)}{6\mathcal{A}_c^p \lambda^2 p} \left(3\kappa\lambda^2(\rho_c + 3P_c) + \frac{4p}{2p-1} \right) \right) r^2, \quad (\text{A.4})$$

$$\mathcal{A}/\mathcal{A}_c = 1 + \left(\frac{\kappa}{6} (3P_c + \rho_c) - \frac{\xi_p(2p-1)}{6\mathcal{A}_c^p \lambda^2 p} \left(3\kappa\lambda^2(\rho_c + P_c) + \frac{4p}{2p-1} \right) \right) r^2, \quad (\text{A.5})$$

$$P = P_c - \frac{P_c + \rho_c}{2} \left(\frac{\kappa}{6} (3P_c + \rho_c) - \frac{\xi_p(2p-1)}{6\mathcal{A}_c^p \lambda^2 p} \left(3\kappa\lambda^2(\rho_c + P_c) + \frac{4p}{2p-1} \right) \right) r^2. \quad (\text{A.6})$$

As a consequence, the kinetic term near the center is given by

$$X = \frac{q^2}{2\mathcal{A}_c} \left(1 - \left(\frac{\kappa(3p-1)(P_c + \rho_c)}{2p} + \frac{1}{\lambda^2} \right) r^2 \right) + \dots \quad (\text{A.7})$$

For $\xi_p > 0$, the local mass $m = (1 - \mathcal{B})/2$ is always positive. By contrast, for sufficiently large ξ_p the sign of $P'(0)$ (respectively $\mathcal{A}'(0)$) can become positive (respectively negative). Imposing that the pressure, like in GR, decreases from the center, i.e. $P'(0) < 0$, yields an upper bound on the parameter ξ_p , which can be expressed as

$$\frac{\xi_p}{\mathcal{A}_c^p} < \frac{\kappa\lambda^2 p (3P_c + \rho_c)}{3\kappa\lambda^2(2p-1)(P_c + \rho_c) + 4p}. \quad (\text{A.8})$$

Finally, from Eq. (3.9) and from the expansions of \mathcal{A} , \mathcal{B} and P , one can evaluate ρ_{eff} at the center of the star,

$$\kappa\rho_{\text{eff},c} \equiv \frac{\xi_p}{\mathcal{A}_c^p} \left(\frac{\kappa(6p-1)(P_c + \rho_c)}{2p} + \frac{2}{\lambda^2} \right), \quad (\text{A.9})$$

where the sign of ρ_{eff} depends on the scalar charge ξ_p . This agrees with the numerical results of Section 4.

B Coefficients b_i for the analytic expression of realistic equations of states

In this section, we give the coefficients b_i that appear in the analytic expression (4.4) for realistic equations of state.

b_i	SLy	b_i	BSk21	BSk22
1	6.22	1	4.857	6.682
2	6.121	2	6.981	5.651
3	0.005925	3	0.00706	0.00459
4	0.16326	4	0.19351	0.14359
5	6.48	5	4.085	2.681
6	11.4971	6	12.065	11.972
7	19.105	7	10.521	13.993
8	0.8938	8	1.5905	1.2904
9	6.54	9	4.104	2.665
10	11.4950	10	-28.726	-27.787
11	-22.775	11	2.0845	2.0140
12	1.5707	12	4.89	4.09
13	4.3	13	14.302	14.135
14	14.08	14	22.881	28.03
15	27.80	15	-1.7690	-1.921
16	-1.653	16	0.989	1.08
17	1.50	17	15.313	14.89
18	14.67	18	0.091	0.098
		19	4.68	4.75
		20	11.65	11.67
		21	-0.086	-0.037
		22	10.0	11.9
		23	14.15	14.10

Table B.1: Coefficients b_i for SLy (from [64]) and coefficients b_i for BSk21 and BSk22 (from [63, 65]).

References

- [1] **LIGO Scientific, Virgo** Collaboration, B. P. Abbott *et al.*, “GWTC-1: A Gravitational-Wave Transient Catalog of Compact Binary Mergers Observed by LIGO and Virgo during the First and Second Observing Runs,” *Phys. Rev. X* **9** no. 3, (2019) 031040, [arXiv:1811.12907 \[astro-ph.HE\]](#). (cit. on p. 2)
- [2] **LIGO Scientific, VIRGO, KAGRA** Collaboration, N. Abac *et al.*, “GWTC-5.0: Observations from the Second Part of the Fourth LIGO-Virgo-KAGRA Observing Run and Updates to the Gravitational-Wave Transient Catalog,” [arXiv:2605.27225 \[gr-qc\]](#). (cit. on p. 2)
- [3] **Event Horizon Telescope** Collaboration, D. Psaltis *et al.*, “Gravitational Test Beyond the First Post-Newtonian Order with the Shadow of the M87 Black Hole,” *Phys. Rev. Lett.* **125** no. 14, (2020) 141104, [arXiv:2010.01055 \[gr-qc\]](#). (cit. on p. 2)
- [4] G. Raaijmakers *et al.*, “Constraining the dense matter equation of state with joint analysis of NICER and LIGO/Virgo measurements,” *Astrophys. J. Lett.* **893** no. 1, (2020) L21, [arXiv:1912.11031 \[astro-ph.HE\]](#). (cit. on p. 2)
- [5] **ET** Collaboration, A. Abac *et al.*, “The Science of the Einstein Telescope,” *JCAP* **03** (2026) 081, [arXiv:2503.12263 \[gr-qc\]](#). (cit. on p. 2)
- [6] **LISA** Collaboration, P. Amaro-Seoane *et al.*, “Laser Interferometer Space Antenna,” [arXiv:1702.00786 \[astro-ph.IM\]](#). (cit. on p. 2)
- [7] **LIGO Scientific, VIRGO, KAGRA** Collaboration, A. G. Abac *et al.*, “GWTC-4.0: Tests of General Relativity. I. Overview and General Tests,” [arXiv:2603.19019 \[gr-qc\]](#). (cit. on p. 2)
- [8] **LIGO Scientific, Virgo** Collaboration, R. Abbott *et al.*, “GW190814: Gravitational Waves from the Coalescence of a 23 Solar Mass Black Hole with a 2.6 Solar Mass Compact Object,” *Astrophys. J. Lett.* **896** no. 2, (2020) L44, [arXiv:2006.12611 \[astro-ph.HE\]](#). (cit. on pp. 2 and 3)
- [9] **LIGO Scientific, KAGRA, VIRGO** Collaboration, A. G. Abac *et al.*, “Observation of Gravitational Waves from the Coalescence of a 2.5–4.5 M_{\odot} Compact Object and a Neutron Star,” *Astrophys. J. Lett.* **970** no. 2, (2024) L34, [arXiv:2404.04248 \[astro-ph.HE\]](#). (cit. on pp. 2 and 3)
- [10] K. Huang, J. Hu, Y. Zhang, and H. Shen, “The possibility of the secondary object in GW190814 as a neutron star,” *Astrophys. J.* **904** no. 1, (2020) 39, [arXiv:2008.04491 \[nucl-th\]](#). (cit. on p. 2)
- [11] I. Bombaci, A. Drago, D. Logoteta, G. Pagliara, and I. Vidaña, “Was GW190814 a Black Hole–Strange Quark Star System?,” *Phys. Rev. Lett.* **126** no. 16, (2021) 162702, [arXiv:2010.01509 \[nucl-th\]](#). (cit. on p. 2)
- [12] X. Zhou, A. Li, and B.-A. Li, “ R -mode Stability of GW190814’s Secondary Component as a Supermassive and Superfast Pulsar,” *Astrophys. J.* **910** no. 1, (2021) 62, [arXiv:2011.11934 \[astro-ph.HE\]](#). (cit. on p. 2)

- [13] E. R. Most, L. J. Papenfort, L. R. Weih, and L. Rezzolla, “A lower bound on the maximum mass if the secondary in GW190814 was once a rapidly spinning neutron star,” *Mon. Not. Roy. Astron. Soc.* **499** no. 1, (2020) L82–L86, [arXiv:2006.14601 \[astro-ph.HE\]](#). (cit. on p. 2)
- [14] A. Kanakis-Pegios, P. S. Koliogiannis, and C. C. Moustakidis, “Probing the Nuclear Equation of State from the Existence of a $\sim 2.6 M_{\odot}$ Neutron Star: The GW190814 Puzzle,” *Symmetry* **13** no. 2, (2021) 183, [arXiv:2012.09580 \[astro-ph.HE\]](#). (cit. on p. 2)
- [15] A. Nathanail, E. R. Most, and L. Rezzolla, “GW170817 and GW190814: tension on the maximum mass,” *Astrophys. J. Lett.* **908** no. 2, (2021) L28, [arXiv:2101.01735 \[astro-ph.HE\]](#). (cit. on p. 2)
- [16] D. Langlois and K. Noui, “Degenerate higher derivative theories beyond Horndeski: evading the Ostrogradski instability,” *JCAP* **1602** no. 02, (2016) 034, [arXiv:1510.06930 \[gr-qc\]](#). (cit. on pp. 3 and 4)
- [17] D. Langlois and K. Noui, “Hamiltonian analysis of higher derivative scalar-tensor theories,” *JCAP* **1607** no. 07, (2016) 016, [arXiv:1512.06820 \[gr-qc\]](#). (cit. on p. 3)
- [18] J. Ben Achour, M. Crisostomi, K. Koyama, D. Langlois, K. Noui, and G. Tasinato, “Degenerate higher order scalar-tensor theories beyond Horndeski up to cubic order,” *JHEP* **12** (2016) 100, [arXiv:1608.08135 \[hep-th\]](#). (cit. on p. 3)
- [19] D. Langlois, “Dark energy and modified gravity in degenerate higher-order scalar–tensor (DHOST) theories: A review,” *Int. J. Mod. Phys. D* **28** no. 05, (2019) 1942006, [arXiv:1811.06271 \[gr-qc\]](#). (cit. on p. 3)
- [20] T. Kobayashi, “Horndeski theory and beyond: a review,” *Rept. Prog. Phys.* **82** no. 8, (2019) 086901, [arXiv:1901.07183 \[gr-qc\]](#). (cit. on p. 3)
- [21] A. Bakopoulos, C. Charmousis, P. Kanti, N. Lecoeur, and T. Nakas, “Black holes with primary scalar hair,” *Phys. Rev. D* **109** no. 2, (2024) 024032, [arXiv:2310.11919 \[gr-qc\]](#). (cit. on pp. 3, 5, 10, 24, and 25)
- [22] O. Baake, A. Cisterna, M. Hassaine, and U. Hernandez-Vera, “Endowing black holes with beyond-Horndeski primary hair: An exact solution framework for scalarizing in every dimension,” *Phys. Rev. D* **109** no. 6, (2024) 064024, [arXiv:2312.05207 \[hep-th\]](#). (cit. on pp. 3, 5, 6, and 24)
- [23] A. Bakopoulos, N. Chatzifotis, and T. Nakas, “Compact objects with primary hair in shift and parity symmetric beyond Horndeski gravities,” *Phys. Rev. D* **110** no. 2, (2024) 024044, [arXiv:2312.17198 \[gr-qc\]](#). (cit. on pp. 3, 4, 5, 6, and 24)
- [24] E. Babichev and C. Charmousis, “Dressing a black hole with a time-dependent Galileon,” *JHEP* **08** (2014) 106, [arXiv:1312.3204 \[gr-qc\]](#). (cit. on p. 3)
- [25] H. Candan, K. Noui, and D. Langlois, “Slowly rotating Black Holes in DHOST Theories,” [arXiv:2512.17614 \[gr-qc\]](#). (cit. on p. 3)
- [26] A. Bakopoulos, N. Chatzifotis, and T. Karakasis, “Thermodynamics of black holes featuring primary scalar hair,” *Phys. Rev. D* **110** no. 10, (2024) L101502, [arXiv:2404.07522 \[hep-th\]](#). (cit. on p. 3)

- [27] A. Bakopoulos, T. Karakasis, and E. Papantonopoulos, “Thermodynamics of stealth black holes,” *Phys. Rev. D* **111** no. 2, (2025) 024065, [arXiv:2410.14451 \[hep-th\]](#). (cit. on p. 3)
- [28] C. Erices and M. Fathi, “Thermodynamic and observational constraints on black holes with primary hair in Beyond Horndeski gravity: Stability and shadows,” *JCAP* **01** (2025) 016, [arXiv:2409.07312 \[gr-qc\]](#). (cit. on p. 3)
- [29] M. Fathi, “Effect of primary scalar hair on black hole’s strong lensing in Beyond Horndeski gravity,” *Phys. Dark Univ.* **50** (2025) 102069, [arXiv:2502.19155 \[gr-qc\]](#). (cit. on p. 3)
- [30] K. Nozari, M. Hajebrahimi, S. Saghafi, G. Mustafa, and E. N. Saridakis, “Rotating Black Holes with Primary Scalar Hair: Shadow Signatures in Beyond Horndeski Gravity,” [arXiv:2602.16237 \[gr-qc\]](#). (cit. on p. 3)
- [31] S. Sirera and J. Noller, “Stability and quasinormal modes for black holes with time-dependent scalar hair,” *Phys. Rev. D* **111** no. 4, (2025) 044067, [arXiv:2408.01720 \[gr-qc\]](#). (cit. on p. 3)
- [32] G. Antoniou, T. D. Pappas, and P. Kanti, “Greybody factors in scalar-tensor gravity and beyond,” *Phys. Rev. D* **112** no. 8, (2025) 084013, [arXiv:2507.17329 \[gr-qc\]](#). (cit. on p. 3)
- [33] C. Montagnon, *Quasi-Normal Modes of Black Holes in Quantum Gravity*. PhD thesis, Lyon, Ecole Normale Supérieure, 2025. (cit. on p. 3)
- [34] S. S. Lahoz, *Black hole ringdown tests of gravity*. PhD thesis, University of Portsmouth, 2025. [arXiv:2510.17600 \[gr-qc\]](#). (cit. on p. 3)
- [35] R. Konoplya, O. Stashko, and Z. Stuchlík, “Quasinormal Modes and Hawking Radiation of Black Holes with Primary Scalar Hair,” [arXiv:2606.16125 \[gr-qc\]](#). (cit. on p. 3)
- [36] C. Charmousis, S. Iteanu, D. Langlois, and K. Noui, “Axial perturbations of black holes with primary scalar hair,” *JCAP* **05** (2025) 102, [arXiv:2503.22348 \[gr-qc\]](#). (cit. on pp. 3, 4, 5, 6, 7, and 24)
- [37] C. Charmousis, S. Iteanu, D. Langlois, and K. Noui, “Radial Perturbations of Black Holes in DHOST Theories,” [arXiv:2606.25972 \[gr-qc\]](#). (cit. on pp. 3 and 4)
- [38] T. Damour and G. Esposito-Farese, “Nonperturbative strong field effects in tensor - scalar theories of gravitation,” *Phys. Rev. Lett.* **70** (1993) 2220–2223. (cit. on p. 3)
- [39] A. Cisterna, T. Delsate, and M. Rinaldi, “Neutron stars in general second order scalar-tensor theory: The case of nonminimal derivative coupling,” *Phys. Rev. D* **92** no. 4, (2015) 044050, [arXiv:1504.05189 \[gr-qc\]](#). (cit. on p. 3)
- [40] A. Cisterna, T. Delsate, L. Ducobu, and M. Rinaldi, “Slowly rotating neutron stars in the nonminimal derivative coupling sector of Horndeski gravity,” *Phys. Rev. D* **93** no. 8, (2016) 084046, [arXiv:1602.06939 \[gr-qc\]](#). (cit. on p. 3)
- [41] E. Babichev, K. Koyama, D. Langlois, R. Saito, and J. Sakstein, “Relativistic Stars in Beyond Horndeski Theories,” *Class. Quant. Grav.* **33** no. 23, (2016) 235014, [arXiv:1606.06627 \[gr-qc\]](#). (cit. on p. 3)
- [42] J. Sakstein, E. Babichev, K. Koyama, D. Langlois, and R. Saito, “Towards Strong Field Tests of Beyond Horndeski Gravity Theories,” *Phys. Rev.* **D95** no. 6, (2017) 064013, [arXiv:1612.04263 \[gr-qc\]](#). (cit. on p. 3)

- [43] E. Babichev, C. Charmousis, and A. Leibel, “Black holes and stars in Horndeski theory,” *Class. Quant. Grav.* **33** no. 15, (2016) 154002, [arXiv:1604.06402 \[gr-qc\]](#). (cit. on pp. 3 and 5)
- [44] A. Leibel, E. Babichev, and C. Charmousis, “A no-hair theorem for stars in Horndeski theories,” *JCAP* **1707** no. 07, (2017) 037, [arXiv:1706.04989 \[gr-qc\]](#). (cit. on p. 3)
- [45] J. Chagoya and G. Tasinato, “Compact objects in scalar-tensor theories after GW170817,” *JCAP* **1808** no. 08, (2018) 006, [arXiv:1803.07476 \[gr-qc\]](#). (cit. on p. 3)
- [46] T. Kobayashi and T. Hiramatsu, “Relativistic stars in degenerate higher-order scalar-tensor theories after GW170817,” *Phys. Rev. D* **97** no. 10, (2018) 104012, [arXiv:1803.10510 \[gr-qc\]](#). (cit. on pp. 3 and 12)
- [47] H. Ogawa, T. Kobayashi, and K. Koyama, “Relativistic stars in a cubic Galileon Universe,” *Phys. Rev. D* **101** no. 2, (2020) 024026, [arXiv:1911.01669 \[gr-qc\]](#). (cit. on p. 3)
- [48] G. Ventagli, G. Antoniou, A. Leibel, and T. P. Sotiriou, “Neutron star scalarization with Gauss-Bonnet and Ricci scalar couplings,” [arXiv:2111.03644 \[gr-qc\]](#). (cit. on p. 3)
- [49] M. Minamitsuji and S. Tsujikawa, “Stability of neutron stars in Horndeski theories with Gauss-Bonnet couplings,” *Phys. Rev. D* **106** no. 6, (2022) 064008, [arXiv:2207.04461 \[gr-qc\]](#). (cit. on p. 3)
- [50] A. Saavedra, G. Rubilar, O. Fierro, M. Gammon, and R. B. Mann, “Neutron stars in 4D Einstein-Gauss-Bonnet gravity,” *Phys. Rev. D* **111** no. 6, (2025) 064071, [arXiv:2412.15459 \[gr-qc\]](#). (cit. on p. 3)
- [51] R. F. Diedrichs, S. Tsujikawa, and K. Yagi, “Tidal Love numbers of neutron stars in Horndeski theories,” *Phys. Rev. D* **112** no. 4, (2025) 044023, [arXiv:2501.07998 \[gr-qc\]](#). (cit. on p. 3)
- [52] T. Kobayashi, “Gravitomagnetic tidal response of relativistic stars in partially screened scalar-tensor theories,” *Phys. Rev. D* **111** no. 8, (2025) 084053, [arXiv:2501.10659 \[gr-qc\]](#). (cit. on pp. 3 and 12)
- [53] H. Lu and Y. Pang, “Horndeski gravity as $D \rightarrow 4$ limit of Gauss-Bonnet,” *Phys. Lett. B* **809** (2020) 135717, [arXiv:2003.11552 \[gr-qc\]](#). (cit. on p. 3)
- [54] R. A. Hennigar, D. Kubizňák, R. B. Mann, and C. Pollack, “On taking the $D \rightarrow 4$ limit of Gauss-Bonnet gravity: theory and solutions,” *JHEP* **07** (2020) 027, [arXiv:2004.09472 \[gr-qc\]](#). (cit. on p. 3)
- [55] P. G. S. Fernandes, P. Carrilho, T. Clifton, and D. J. Mulryne, “The 4D Einstein–Gauss–Bonnet theory of gravity: a review,” *Class. Quant. Grav.* **39** no. 6, (2022) 063001, [arXiv:2202.13908 \[gr-qc\]](#). (cit. on p. 3)
- [56] C. Charmousis, A. Leibel, E. Smyrniotis, and N. Stergioulas, “Astrophysical constraints on compact objects in 4D Einstein-Gauss-Bonnet gravity,” *JCAP* **02** no. 02, (2022) 033, [arXiv:2109.01149 \[gr-qc\]](#). (cit. on p. 3)
- [57] J. Ben Achour, D. Langlois, and K. Noui, “Degenerate higher order scalar-tensor theories beyond Horndeski and disformal transformations,” *Phys. Rev. D* **93** no. 12, (2016) 124005, [arXiv:1602.08398 \[gr-qc\]](#). (cit. on p. 4)

- [58] J. Gleyzes, D. Langlois, F. Piazza, and F. Vernizzi, “Healthy theories beyond Horndeski,” *Phys. Rev. Lett.* **114** no. 21, (2015) 211101, [arXiv:1404.6495 \[hep-th\]](#). (cit. on p. 4)
- [59] J. Gleyzes, D. Langlois, F. Piazza, and F. Vernizzi, “Exploring gravitational theories beyond Horndeski,” *JCAP* **1502** (2015) 018, [arXiv:1408.1952 \[astro-ph.CO\]](#). (cit. on p. 4)
- [60] G. W. Horndeski, “Second-order scalar-tensor field equations in a four-dimensional space,” *Int. J. Theor. Phys.* **10** (1974) 363–384. (cit. on p. 4)
- [61] L. Hui and A. Nicolis, “No-Hair Theorem for the Galileon,” *Phys. Rev. Lett.* **110** (2013) 241104, [arXiv:1202.1296 \[hep-th\]](#). (cit. on p. 5)
- [62] B. Schutz, *A first course in general relativity*. Cambridge university press, 2022. (cit. on p. 9)
- [63] P. Haensel and A. Y. Potekhin, “Analytical representations of unified equations of state of neutron-star matter,” *Astron. Astrophys.* **428** (2004) 191–197, [arXiv:astro-ph/0408324](#). (cit. on pp. 16 and 27)
- [64] A. Potekhin, A. Fantina, N. Chamel, J. Pearson, and S. Goriely, “Analytical representations of unified equations of state for neutron-star matter,” *Astron. Astrophys.* **560** (2013) A48, [arXiv:1310.0049 \[astro-ph.SR\]](#). (cit. on pp. 16 and 27)
- [65] J. M. Pearson, N. Chamel, A. Y. Potekhin, A. F. Fantina, C. Ducoin, A. K. Dutta, and S. Goriely, “Unified equations of state for cold non-accreting neutron stars with Brussels–Montreal functionals – I. Role of symmetry energy,” *Mon. Not. Roy. Astron. Soc.* **481** no. 3, (2018) 2994–3026, [arXiv:1903.04981 \[astro-ph.HE\]](#). [Erratum: *Mon. Not. Roy. Astron. Soc.* 486, 768 (2019)]. (cit. on pp. 16 and 27)
- [66] E. Babichev and A. Lehébel, “The sound of DHOST,” *JCAP* **12** (2018) 027, [arXiv:1810.09997 \[gr-qc\]](#). (cit. on p. 25)
- [67] I. D. Saltas and I. Lopes, “Obtaining Precision Constraints on Modified Gravity with Helioseismology,” *Phys. Rev. Lett.* **123** no. 9, (2019) 091103, [arXiv:1909.02552 \[astro-ph.CO\]](#). (cit. on p. 25)
- [68] G. Ventagli, P. G. S. Fernandes, A. Maselli, A. Padilla, and T. P. Sotiriou, “Neutron stars and the cosmological constant problem,” *Phys. Rev. D* **111** no. 2, (2025) 024001, [arXiv:2404.19012 \[gr-qc\]](#). (cit. on p. 25)
- [69] C. Charmousis, P. G. S. Fernandes, and M. Hassaine, “Proca theory of four-dimensional regularized Gauss-Bonnet gravity and black holes with primary hair,” *Phys. Rev. D* **111** no. 12, (2025) 124008, [arXiv:2504.13084 \[gr-qc\]](#). (cit. on p. 25)
- [70] P. G. S. Fernandes, “Exact analytic rotating black-hole solutions with primary hair,” [arXiv:2601.21163 \[gr-qc\]](#). (cit. on p. 25)
- [71] C. Charmousis, P. G. S. Fernandes, and M. Hassaine, “Effective cosmological constant as black hole primary hair,” *Phys. Rev. D* **113** no. 12, (2026) 124063, [arXiv:2603.25598 \[gr-qc\]](#). (cit. on p. 25)
- [72] L. Heisenberg, “Generalised Proca Theories,” in *52nd Rencontres de Moriond on Gravitation*, pp. 233–241. 2017. [arXiv:1705.05387 \[hep-th\]](#). (cit. on p. 25)

- [73] J. Beltran Jimenez and T. S. Koivisto, “Extended Gauss-Bonnet gravities in Weyl geometry,” *Class. Quant. Grav.* **31** (2014) 135002, [arXiv:1402.1846 \[gr-qc\]](#). (cit. on p. 25)
- [74] S. Bahamonde and M. Bañados, “An exact five dimensional Weyl-geometry Gauss-Bonnet black hole,” *Phys. Lett. B* **869** (2025) 139869, [arXiv:2504.02230 \[gr-qc\]](#). (cit. on p. 25)